CM^2

MAGAZINE

第 63 期

南方科技大学海洋磁学中心主编

https://cm2.sustech.edu.cn/

创刊词

海洋是生命的摇篮，是文明的纽带。地球上最早的生命诞生于海洋，海洋里的生命最终进化成了人类，人类的文化融合又通过海洋得以实现。人因海而兴。

人类对海洋的探索从未停止。从远古时代美丽的神话传说，到麦哲伦的全球航行，再到现代对大洋的科学钻探计划，海洋逐渐从人类敬畏崇拜幻想的精神寄托演变成可以开发利用与科学研究的客观存在。其中，上个世纪与太空探索同步发展的大洋科学钻探计划将人类对海洋的认知推向了崭新的纬度：深海（deep sea）与深时（deep time）。大洋钻探计划让人类知道，奔流不息的大海之下，埋藏的却是亿万年的地球历史。它们记录了地球板块的运动，从而使板块构造学说得到证实；它们记录了地球环境的演变，从而让古海洋学方兴未艾。

在探索海洋的悠久历史中，从大航海时代的导航，到大洋钻探计划中不可或缺的磁性地层学，磁学发挥了不可替代的作用。这不是偶然，因为从微观到宏观，磁性是最基本的物理属性之一，可以说，万物皆有磁性。基于课题组的学科背景和对海洋的理解，我们对海洋的探索以磁学为主要手段，海洋磁学中心因此而生。

海洋磁学中心，简称 CM^2，一为其全名"Centre for Marine Magnetism"的缩写，另者恰与爱因斯坦著名的质能方程 $E = MC^2$ 对称，借以表达我们对科学巨匠的敬仰和对科学的不懈追求。

然而科学从来不是单打独斗的产物。我们以磁学为研究海洋的主攻利器，但绝不仅限于磁学。凡与磁学相关的领域均是我们关注的重点。为了跟踪反映国内外地球科学特别是与磁学有关的地球科学领域的最新研究进展，海洋磁学中心特地主办 CM^2 Magazine，以期与各位地球科学工作者相互交流学习、合作共进！

"海洋孕育了生命，联通了世界，促进了发展"。21 世纪是海洋科学的时代，由陆向海，让我们携手迈进中国海洋科学的黄金时代。

目　　录

文献速递

1. 全新世以来全球古地磁场变化中的特征周期

翻译人：柳加波 liujb@sustech.edu.cn

摘要：了解不同时间尺度上的地磁场长期变化，对于了解维持地磁场的机制具有重要作用，并有助于建立发电机理论的约束条件。我们将研究重点放在千年和百年时间尺度上的长期变化中，以寻找最近一万年内的特征时期。频率研究是通过应用信号分析中常用的三种技术：傅立叶变换，经验模态分解和小波分析。基于这些频率研究方法，我们对四个最新的全球古磁场模型（SHA.DIF.14k、CALS10k.2、BIGMUDI4k 和 SHAWQ2k）进行了分析。

地磁场能量的短期变化显示出大约 2000 年、1000-1400 年、600-800 年和 250-400 年的重复周期。600-800 年左右的特征时间在所有古地磁模型中都得到了很好的确定，它主要与轴向偶极子和轴向八极子项有关，但在赤道偶极子（非轴向偶极子）中也可以观察到。除此周期外，在 SHA.DIF.14k、CALS10k.2 和 BIGMUDI4k 模型中，赤道偶极子和四极子项中发现了更长的特征时间，大约为 1000-1400 年。而 2000 年的时间周期仅在 SHA.DIF.14k 和 CALS10k.2 的总场能得到很好的确定。最新时期的最详细的古地磁模型也可发现约 250-400 年的最短特征周期时间。

地磁能的长期变化只能在轴向偶极子中观察到。在 SHA.DIF.14k 和 CALS10k.2 中都发现了大约 7000 年的特征周期。这个长周期与偶极子场中的两个衰变以及强度增加的周期有关。最老的衰减发生在公元前 7000 年至 4500 年之间，而目前的衰减始于公元前 100 年左右。作为一个连续衰减的组合，我们模拟了 4500 BCE 至今的变化。该连续衰减表征了地磁场的扩散项（diffusion term），而一个脉冲则增强了磁场的强度。结果表明，特征扩散时间约为 11000‐15000 年，这与地球动力学理论中使用的偶极子场的扩散时间一致。

ABSTRACT: The knowledge of the secular variation of the geomagnetic field at different time scales is important to determine the mechanisms that maintain the geomagnetic field and can help to establish constraints in dynamo theories. We have focused our study on the secular variation at millennial and centennial time scale searching for characteristic periods during the last 10 kyr. The frequency study was performed using four recent updated global paleomagnetic field reconstructions (SHA.DIF.14k, CALS10k.2, BIGMUDI4k and SHAWQ2k) by applying three techniques commonly used in signal analysis: the Fourier transform, the Empirical Mode Decomposition, and the wavelet analysis.

Short-term variability of the geomagnetic field energy shows recurrent periods of around 2000, 1000–1400, and 600–800 and 250–400 years. The characteristic time around 600–800 years is well determined in all paleomagnetic reconstructions and it is mostly related to the axial dipole and axial octupole terms, but also observable in the equatorial dipole. In addition to this period, longer characteristic times of around 1000–1400 years are found particularly in the equatorial dipole and quadrupole terms in SHA.DIF.14k, CALS10k.2 and BIGMUDI4k while the 2000 year period is only well determined in the total geomagnetic field energy of SHA.DIF.14k and CALS10k.2. The most detailed paleoreconstructions for younger times also detect shortest characteristic times of around 250–400 years.

The long-term variation of the geomagnetic energy is only observable in the axial dipole. A characteristic period of around 7000 years in both SHA.DIF.14k and CALS10k.2 has been found. This long period is related to two decays in the dipole field and a period of increasing intensity. The oldest decay took place between 7000 BCE and 4500 BCE and the present decay that started around 100 BCE. We have modeled the 4500 BCE up to present variation as a combination of a continuous decay, representing the diffusion term of the geomagnetic field, and one pulse that reinforces the strength of the field. Results show a characteristic diffusion time of around 11,000–15,000 years, which is compatible with the diffusion times of the dipole field used in geodynamo theories.
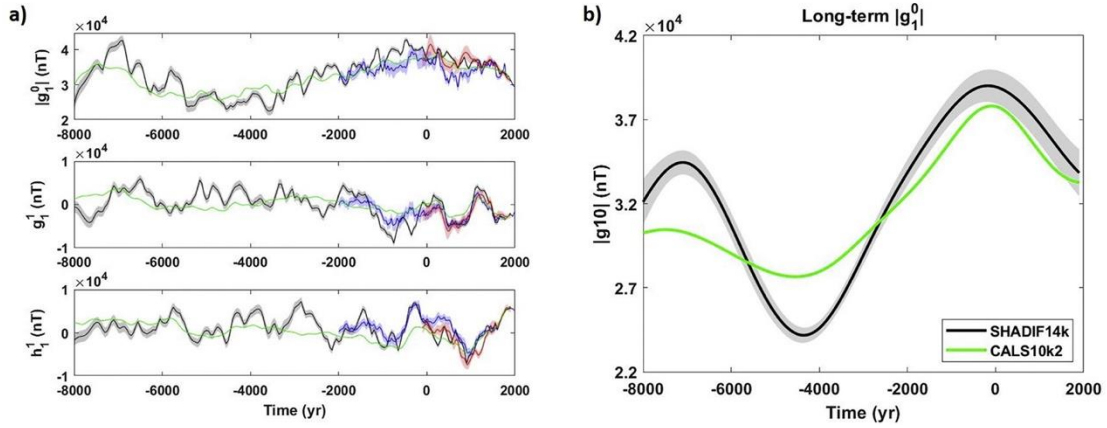
2

Figure 1. a) Temporal evolution of the first three Gauss coefficients: absolute value of g_1^0 (top), g_1^1 (middle) and h_1^1 (bottom) for SHA.DIF.14k (black), CALS10k.2 (green), BIGMUDI4k (blue) and SHAWQ2k (red). b) Long-term of the $|g_1^0|$ from SHA.DIF.14k (black) with error band and CALS10k.2 (green) without it as it does not provide Gauss coefficient uncertainties. (For interpretation of the references to color in this figure legend, the reader is referred to the web version of this article.)
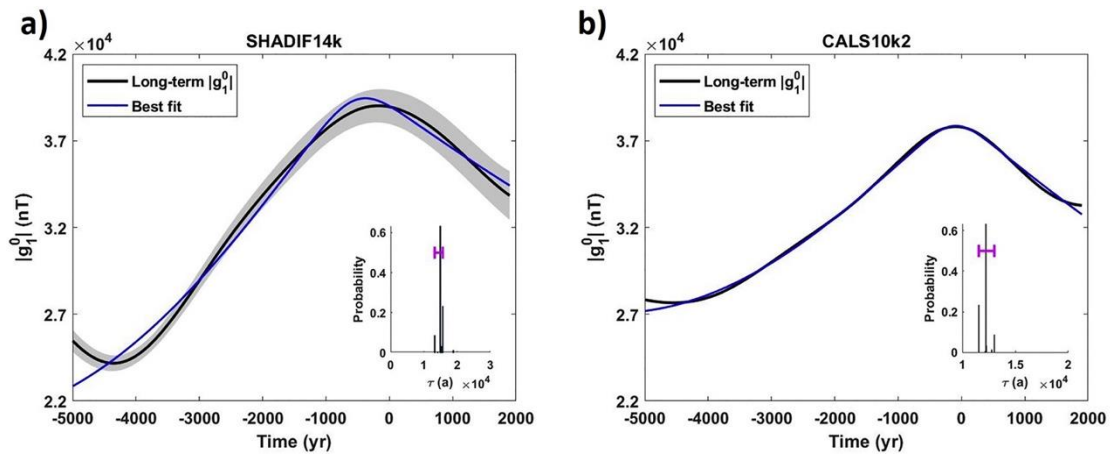

Figure 2. Best fit (blue) for the long-term of $|g_1^0|$ (black) in SHA.DIF.14 k (left) and CALS10k.2 (right) for the two scenarios explained in the main text: Case 1 (top) and Case 2 (bottom). Each figure also presents the most probable values of τ (years) at 95% probability (pink bar) in each case and paleoreconstruction. (For interpretation of the references to color in this figure legend, the reader is referred to the web version of this article.)

2. 冰期南大洋研究：关于南极表面日射量假设与北太平洋地区的对比综述

翻译人：仲义 zhongy@sustech.edu.cn

摘要： 人们普遍认为，南大洋是造成大气浓度较低的一个潜在原因，但是其成因机制还存在争议。以南大洋表层生产力为研究对象，作者回顾了生物地球化学代用指标和碳循环概念，结果整体上支持南极及南大洋亚南极区域在冰期降低 CO_2 的重要作用。在亚南极地区，冰期风尘铁输入促进浮游植物的爆发。而在南极冰期，表层水与次表层水之间水团交换作用减弱，作者将这种状态总结为南极表面"分层隔离"状态。在大多数情况下，这种改变将会阻止今天南极地区生物效应储存的 CO_2 的释放。上一个冰期亚南极铁肥作用与我们从现代观测和实验中获得的认识一致，因此，这个假设在得到证据支持之前就被提出了。相反，在最后一个冰期的气候模拟结果中，南极表层隔离作用既不是直观地，也不是自发产生的。

在本综述中一个更有前瞻性的组成部分中,作者在讨论南极表面分层效应的成因是必须考虑亚北极太平洋表面分层效应的原因，通过该地区反映生产力与营养盐利用率指标显示，在冰期循环过程中上层海洋生物地球化学过程与南极地区较为一致，而在冰消期的发生时间明显不同。在提出南极表面分层效应的启动因素时，我们往往会寻求一种单一的机制来解释南极与亚北极地区的生物地球化学变化。该分析倾向于两个半球间存在西风带相关的上升流作用减弱或者向赤道位置的移动。而这种观点是有争议的，尤其在亚北极地区，证据显示在最后一个冰期，该地区的上层水团的通风作用得到了增强。作者对于南极和亚北极的记录提出一种可能性解释。在这两个地区，随着西风带驱动的上升流减弱，营养物质可能已经从上层水团中释放出来，并伴随着等密度线向极地的下降。而在南极，这将会导致营养组分降低和新的深层水形成减慢，这两种都会导致大气中 CO_2 含量的降低。通过这些效应，南极上升流的减弱可能会促进深层水上升流作用扩展到低纬度密度跃层，并保持密度跃层的水分和营

养供给，并最终导致（1）冰期生产力升高；（2）平衡由于北大西洋中层水形成导致密度跃层中水分流失。从深海到表层返回路线与 Broecker's (1991)提出的大洋传送带理论一直，但是该理论适用于冰河时代，而非现代海洋。

ABSTRACT: The Southern Ocean is widely recognized as a potential cause of the lower atmospheric concentration of CO_2 during ice ages, but the mechanism is debated. Focusing on the Southern Ocean surface, we review biogeochemical paleoproxy data and carbon cycle concepts that together favor the view that both the Antarctic and Subantarctic Zones (AZ and SAZ) of the Southern Ocean played roles in lowering ice age CO_2 levels. In the SAZ, the data indicate dust-driven iron fertilization of phytoplankton growth during peak ice age conditions. In the ice age AZ, the area-normalized exchange of water between the surface and subsurface appears to have been reduced, a state that we summarize as "isolation" of the AZ surface. Under most scenarios, this change would have stemmed the leak of biologically stored CO_2 that occurs in the AZ today. SAZ iron fertilization during the last ice age fits with our understanding of ocean processes as gleaned from modern field studies and experiments; indeed, this hypothesis was proposed prior to evidentiary support. In contrast, AZ surface isolation is neither intuitive nor spontaneously generated in climate model simulations of the last ice age.

In a more prospective component of this review, the suggested causes for AZ surface isolation are considered in light of the subarctic North Pacific (SNP), where the paleoproxies of productivity and nutrient consumption indicate similar upper ocean biogeochemical changes over glacial cycles, although with different timings at deglaciation. Among the proposed initiators of glacial AZ surface isolation, a single mechanism is sought that can explain the changes in both the AZ and the SNP. The analysis favors a weakening and/or equatorward shift in the upwelling associated with the westerly winds, occurring in both hemispheres. This view is controversial, especially for the SNP, where there is evidence of enhanced upper water column ventilation during the last ice age. We offer an interpretation that may explain key aspects of the AZ and SNP observations. In both regions, with a weakening in westerly wind-driven upwelling, nutrients may have been "mined out" of the upper water column, possibly accompanied by a poleward "slumping" of isopycnals. In the AZ, this would have encouraged declines in both the nutrient content and the formation rate of new deep

water, each of which would have contributed to the lowering of atmospheric CO_2. Through several effects, the reduction in AZ upwelling may have invigorated the upwelling of deep water into the low latitude pycnocline, roughly maintaining the pycnocline's supply of water and nutrients so as to (1) support the high productivity of the glacial SAZ and (2) balance the removal of water from the pycnocline by the formation of Glacial North Atlantic Intermediate Water. The proposed return route from the deep ocean to the surface resembles that of Broecker's (1991) "global ocean conveyor," but applying to the ice age as opposed to the modern ocean.
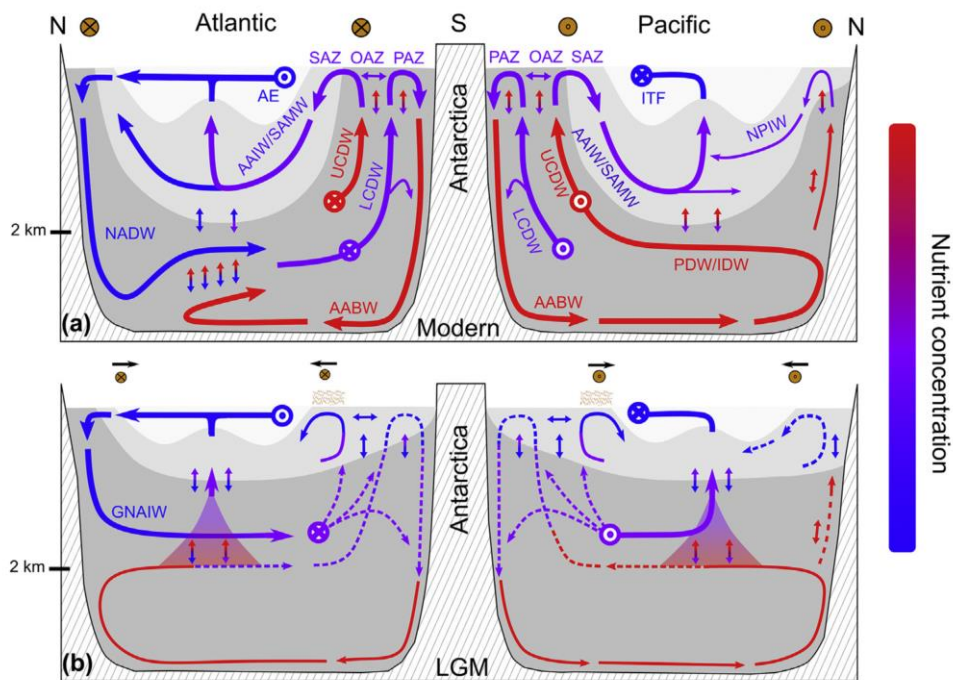

Figure 1. Schematic of the global ocean's interior circulation today (a) and a proposal for the Last Glacial Maximum (b, LGM). Abbreviations are as follows: PAZ, Polar Antarctic Zone; OAZ, Open Antarctic Zone; SAZ, Subantarctic Zone; NADW, North Atlantic Deep Water; GNAIW, Glacial North Atlantic Intermediate Water; PDW, Pacific Deep Water; IDW, Indian Deep Water; UCDW, Upper Circumpolar Deep Water; LCDW, Lower Circumpolar Deep Water; AABW, Antarctic Bottom Water; AAIW, Antarctic Intermediate Water; SAMW, Subantarctic Mode Water; ITF, Indonesian Throughflow; AE, Agulhas Eddies (ITF and AE return surface water from the Pacific to the Atlantic). Circled points and crosses show water and westerly wind transports out of and into the page, respectively (with the winds as orange circles). Line thickness changes among panels largely denote changes in flow rate, with thin dashed lines representing the greatest declines from modern; in the modern, the thinner flow lines in the SNP denote weaker wind-driven upwelling than in the AZ. Double-direction arrows indicate lateral

mixing between surface PAZ and OAZ in the Southern Ocean, vertical mixing across the base of the mixed layer in the AZ and SNP, and vertical (i.e., diapycnal) mixing in the ocean interior. Line colors indicate nutrient (nitrate phosphate) concentration according to the color scale (red highest and blue lowest). All panels show the global ocean's upper and lower overturning cells (i.e., those beginning in the SAZ and PAZ, respectively); the depiction follows Toggweiler et al. (2006) but shows the interconnection of the cells described by Talley (2013) and highlighted by Ferrari et al. (2014). The gray scale indicates relative water densities, with light gray shading indicating the global pycnocline, the proposed poleward "slumping" of which is shown in (b) for the LGM and is explained in the text. For explanation of (a), see section 2. Additional phenomena in (b) include an equatorward shift and weakening in the westerly winds (black horizontal arrows and wind symbol size reduction) and increased dust-borne iron supply to the SAZ (brown stipples). For further explanation of (b), see sections 6, 7, and 9.
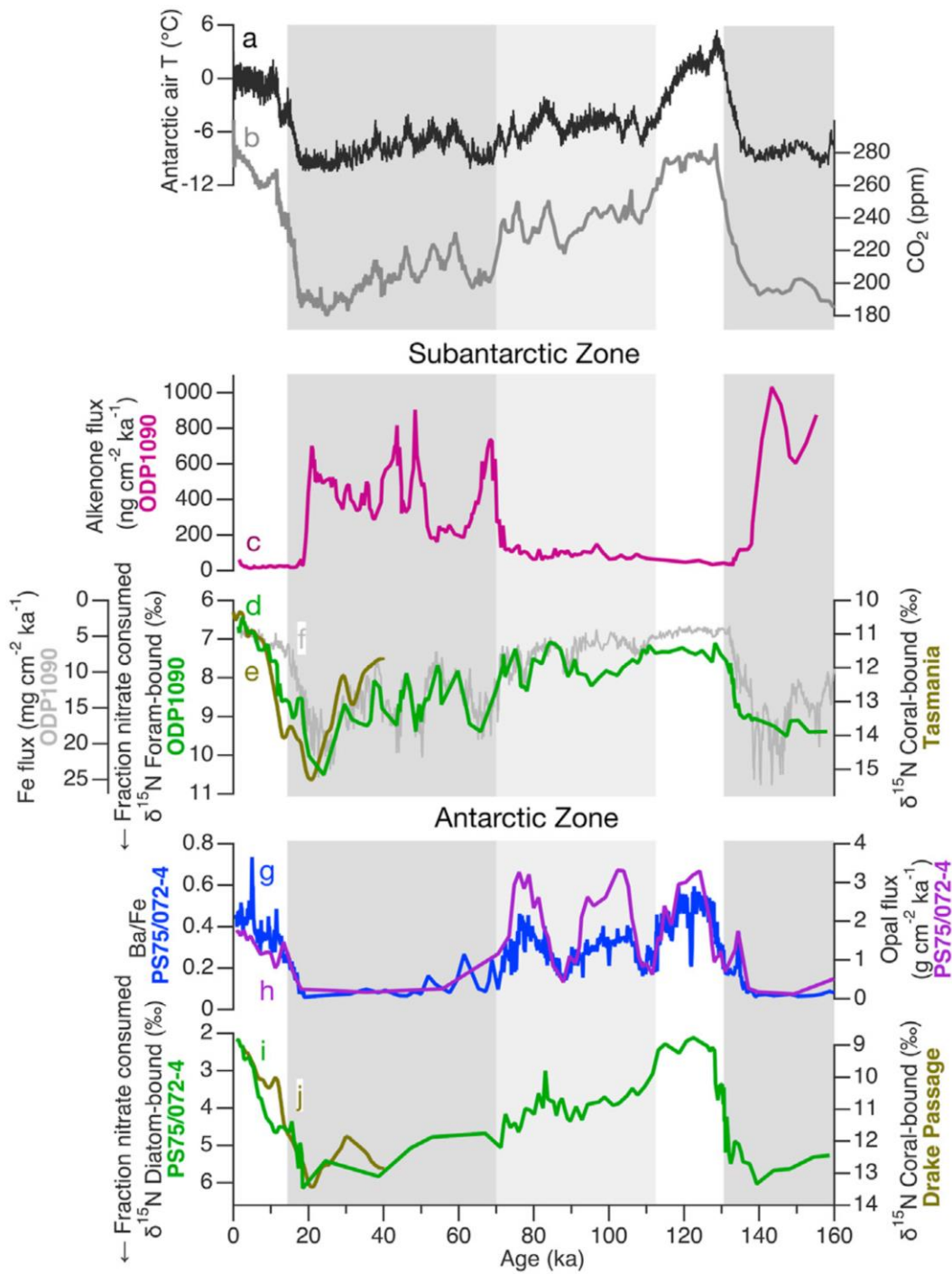
Figure 2. Reconstructions of biogenic flux and fossil-bound nitrogen isotopic composition from the SAZ and AZ over the last full glacial cycle. The Antarctic air temperature reconstruction from EPICA Dome C ice deuterium is shown in black (a; Jouzel et al., 2007), and the atmospheric CO_2 reconstruction compiled from Antarctic ice cores is shown in gray (b; Lüthi et al., 2008). The dark gray background indicates the main glacial intervals MIS 6 and 2e4, the white indicates the full interglacial intervals (MIS

5e and 1), and the light gray indicates a period early in the development of the last ice age (MIS 5a-d). In the SAZ, 230Th-normalized fluxes of alkenones (c, purple) and iron (f, light gray) and foraminifera-bound $d^{15}N$ (d, dark green) are from the Atlantic sector core ODP Site 1090 (Martínez-García et al., 2014). Plotted with the ODP Site 1090 foram-bound $d^{15}N$ is a compilation of deep sea coral-bound $d^{15}N$ from the SAZ south of Tasmania (e, olive; Wang et al., 2017). In the AZ, sediment barium-to-iron ratio (g, blue), 230Th-normalized opal flux (h, purple), and pennate diatom-bound $d^{15}N$ (i, green) are from the Pacific sector core PS75/072-4 (Studer et al., 2015). Coral-bound $d^{15}N$ is also shown from the AZ in the Drake Passage (j, olive; Wang et al., 2017). Throughout, $d^{15}N$ is in permil, referenced to air N2. In the SAZ, both biogenic flux and $d^{15}N$ are higher in glacial stages, suggesting higher export production and more complete nitrate consumption in response to higher dust-borne iron fluxes to the SAZ, supporting the iron fertilization hypothesis first proposed by John Martin. In the AZ, biogenic flux is lower in the glacial stages than interglacial stages, suggesting lower export production, while $d^{15}N$ is higher in glacial stages, suggesting a higher degree of nitrate consumption. The combined changes in these two parameters indicate a reduction in gross nitrate supply to the surface mixed layer during glacial stages.
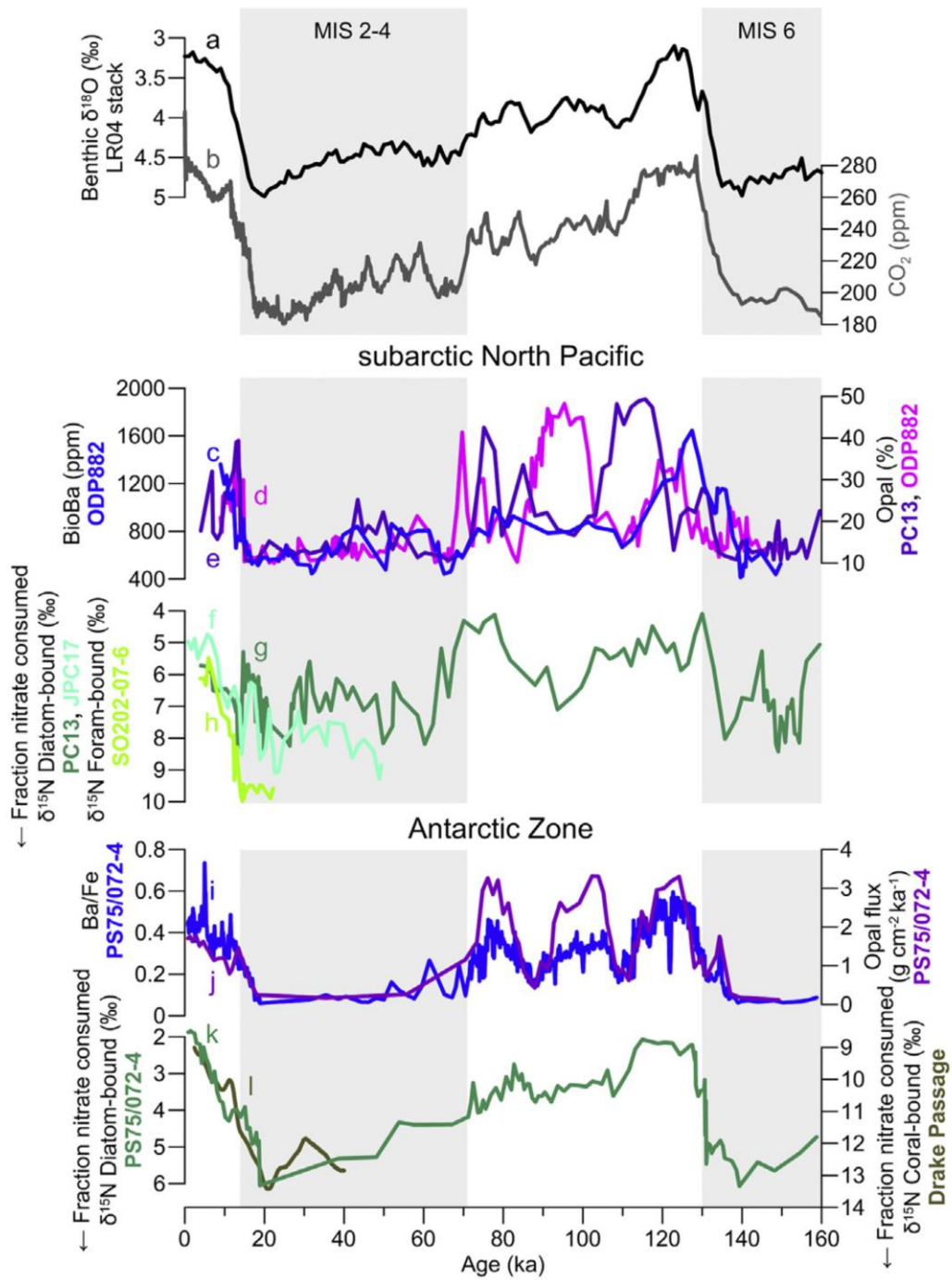
Figure 3. Comparison of reconstructions of biogenic flux and fossil-bound nitrogen isotopic composition from the AZ and western SNP, which argue for reduced nitrate supply in both regions during ice ages. The benthic foraminifera d[18]O stack of Lisiecki and Raymo (2005) is shown in black, and the atmospheric CO_2 reconstruction compiled from Antarctic ice cores is shown in gray (Lüthi et al., 2008). The gray background indicates the main glacial intervals MIS 6 and 2e4, and the white indicates the predominantly interglacial intervals MIS 5 and 1. In the AZ, 230Th-normalized opal accumulation and barium-to-iron

ratio (purple and blue) and pennate diatom-bound d^{15}N (dark green) are from Pacific sector core PS75/072-4 (Studer et al., 2015). Plotted with the diatom-bound d^{15}N is a compilation of deepsea coral-bound d^{15}N from the AZ in the Drake Passage (olive; Wang et al., 2017). In the western SNP, biogenic barium concentration (blue) is from ODP Site 882, biogenic opal concentration records are from ODP Site 882 and Roundabout PC13 (pink and purple), diatombound d^{15}N (dark green) is from PC13, and foraminifera-bound d^{15}N (grass green) is from INOPEX core SO202-07-6 (Jaccard et al., 2005; Brunelle et al., 2010; Ren et al., 2015). Diatom-bound d^{15}N is also shown from Healy-0202 JPC17 in the central Bering Sea back to 50 ka (aqua) (Brunelle et al., 2007). In both regions, biogenic fluxes are lower in glacial stages than interglacial stages, while d^{15}N is higher in glacial stages, the former suggesting lower export production and the latter suggesting a higher degree of nitrate consumption. Following the arguments of François et al. (1997), the combined changes in these two parameters require a reduction in gross nitrate supply to the surface mixed layer during glacial stages. Both SNP diatom-bound d^{15}N records show a local minimum during Heinrich Stadial 1 (HS1) at the end of MIS 2; this minimum does not occur in foraminifera-bound d^{15}N (Ren et al., 2015; see Fig. 6) and appears to be an artifact deriving from sponge spicules due to the very low abundance of diatom opal in this depth interval of the western SNP sediment cores (Studer et al., 2013).
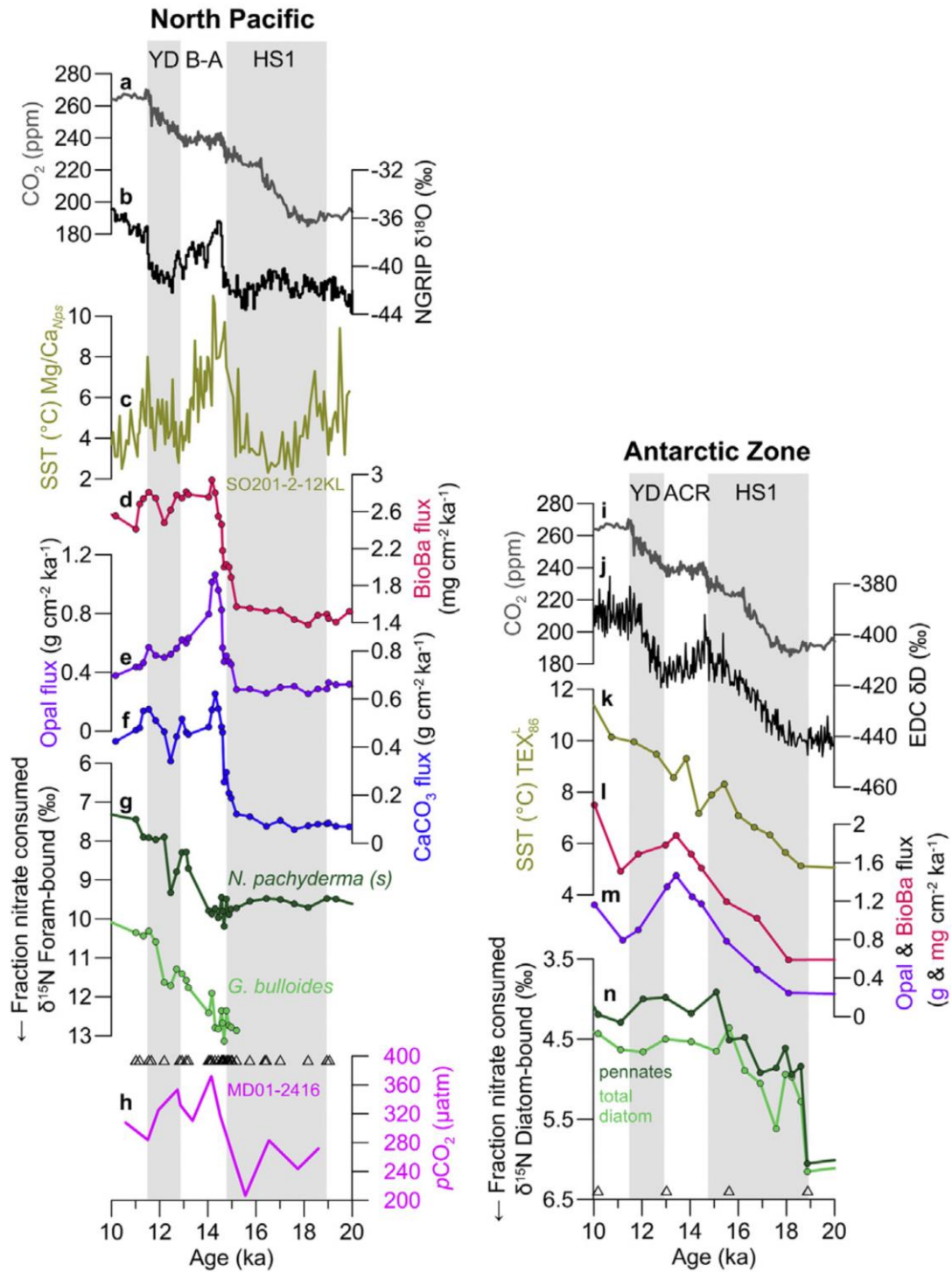
Figure 4. Comparison of reconstructions of biogenic flux and diatom- or foraminiferabound nitrogen isotopic composition from the AZ and western SNP across the last glacial termination (i.e., the last deglaciation). In the AZ (right), 230Th-normalized opal and biogenic barium accumulation (purple and pink), pennate and total diatom-bound d[15]N (dark and light green), and TEX86 L -based sea surface temperature (bronze) are from the same Pacific sector core (PS75/072-4) as shown in Figs. 4 and 5. In

the western SNP (left), 230Th-normalized fluxes of biogenic barium (pink), biogenic opal (purple), and $CaCO_3$ (blue) and the $d^{15}N$ of foraminifera-bound N (N. pachyderma (s) in dark green, G. bulloides in light green) are from core SO202-07-6 (Ren et al., 2015); Mg/Ca-based sea surface temperature (bronze) is from core SO-201-2-12KL (Riethdorf et al., 2013); and boron isotope-based surface water pCO_2 (pink) is from core MD01-2416 (Gray et al., 2018). The ice $d^{18}O$ record from Greenland ice core NGRIP and the ice dD record from Antarctic ice core EPICA Dome C are shown in black on the left and right, reflecting northern and southern hemisphere high latitude air temperature (NGRIP Community Members, 2004; Jouzel et al., 2007). The gray background indicates northern hemisphere cold phases first identified in the circum-North Atlantic (Heinrich Stadial 1 (HS1) and the Younger Dryas (YD)), and the white indicates warmer northern hemisphere intervals (the Bolling-Allerod (BeA), also indicated as the Antarctic Cold Reversal (ACR), and the post-Younger Dryas). Triangles indicate age control points for SO202-07-6 (left) and PS75/072-4 (right) (Studer et al., 2015; Ren et al., 2015). The SO202-07-6 age model is well-resolved (Serno et al., 2015; Ren et al., 2015) and clearly indicates that the deglacial increase in surface/subsurface exchange in the SNP does not occur until the B-A. The SNP d15N decline may have been delayed by subsurface nitrate $d^{15}N$ changes during the B-A (Ren et al., 2015), such that SNP nitrate consumption may have fallen earlier in the B-A than is suggested by the timing of the d15N decline. While the age model at AZ core PS75/072-4 derives largely from planktonic $d^{18}O$ (Studer et al., 2015) and is less certain, the first rise in TEX86Lbased sea surface temperature in the core, when aligned with the warming reflected in Antarctic ice core dD, indicates that the AZ biogeochemical changes began during HS1 and not during the B-A, and this is consistent with other studies (Anderson et al., 2009; Jaccard et al., 2013).
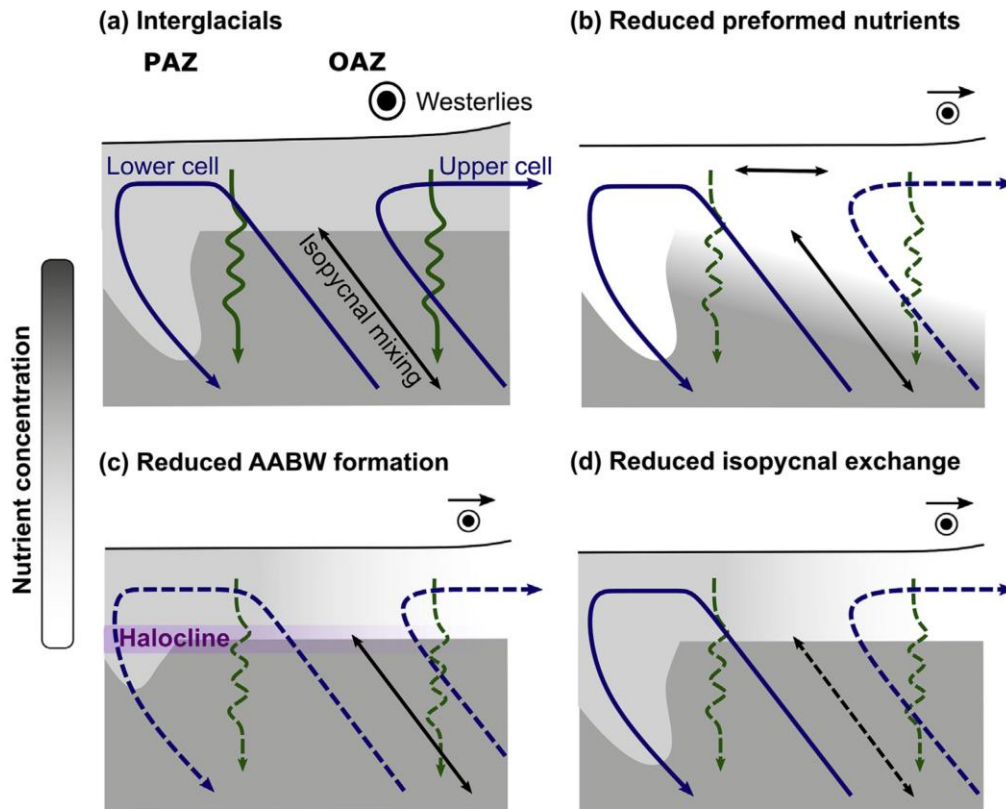
Figure 5. Mechanisms through which a weakening in the upper cell of Southern Ocean circulation could lead to the storage of more CO_2 in the deep ocean during ice ages. Southward is to the left in each panel. Gray shading qualitatively indicates the nutrient (nitrate or phosphate) concentration, and dotted arrows indicate a reduction in magnitude relative to the interglacial condition. (a) The modern condition of strong upper and lower cells and incomplete surface nutrient consumption. (b, c, d) Reduced upper cell strength (dotted lines) relative to the interglacial case, leading to three separable but non-exclusive mechanisms for increased deep CO_2 storage. (b) Lower surface nutrient concentration across the entire AZ, including the PAZ, the region mostly directly ventilating the lower cell, leading to a reduction in the preformed nutrient content of the deep ocean. In the OAZ, nutrients are proposed to have been lowered not only at the surface but also in the shallow subsurface; this is proposed to be the result of "nutrient mining" and/or pycnocline slumping (see text). Export production was apparently reduced throughout the glacial AZ – both the OAZ and the PAZ (thinning and dashing of the wavy green arrows). Thus, for surface nutrients to be low in the glacial PAZ without a decline in overturning in the region, lower-nutrient water must have been mixed in from the OAZ (horizontal bidirectional arrow). Note that the deep ocean maintains high nutrient concentrations, with the preformed nutrient concentration decline

matched by a rise in regenerated nutrients (and thus more CO_2 storage). (c) The increase in the residence time of AZ surface waters may lead to a strengthening of the halocline, which causes a reduction of deep ocean ventilation by the lower cell (Toggweiler et al., 2006; De Boer et al., 2008). In this case, the PAZ may also have experienced a decline in surface nutrient concentration due to its own changes in overturning (i.e., the reduction in nutrient supply from the lower cell). CO_2 leakage from the region would have decreased without a decline in PAZ surface nutrient concentration, but the CO_2 decrease would have been greater with a surface nutrient decline. In (c), the upper and lower cells are shown shifted northward, as this shift may also have helped the PAZ halocline to strengthen (Lawrence et al., 2013). (d) Decreased Ekman transport should have caused a weakening in eddy mixing along interior isopycnals that would have reduced deep ocean ventilation (Abernathey and Ferreira, 2015). Not shown here but shown in Fig. 1 b due to its global scale, an equatorward migration of the westerlies may also have slowed the lower cell by shoaling the deep ocean contact zone between the lower limb of the upper cell and the upper limb of the lower cell, so as to be further above the mixing-inducing features of the seafloor (Watson and Naveira Garabato, 2006; Lund et al., 2011; Ferrari et al., 2014; De Boer and Hogg, 2014). However, our comparison of the AZ with the SNP (Figs. 5 and 6; Table 1) argues that such a deep ocean change did not initiate the ice age surface isolation of the AZ.

3. 全球甲烷释放一半来自高变化性的水环境生态系统

翻译人：蒋晓东 jiangxd@sustech.edu.cn

摘要：甲烷是一种温室效应极强的气体，在控制地球气候演变中发挥了重要作用。自 2007 年以来甲烷浓度显著增大，相关原因并不清楚，主要因为甲烷释放涉及多个物源和复杂的地球化学过程。本研究整合自然环境和人类活动影响下的元数据，分析水环境系统的甲烷通量。改进的自底向上的全球水环境甲烷释放联合来自 15 个水环境系统中散布与迸发的或者植物调和的通量进行研究。我们强调在水生态系统和偏态分布的经验数据之间高变化性的甲烷通量，这使全球估算对统计的假设和抽样设计变得敏感。我们发现水生态系统对全球人为或自然来源的甲烷释放的贡献量可达到平均值 53%或中值为 41%。数据表明甲烷释放量从自然环境到受干扰的水生态系统逐渐增多，从海岸到淡水系统也在增多。我们认为城市化、富营养化、正向的气候反馈等因素很可能使水环境甲烷释放增强，土地管理的变化可作为潜在的减少水环境甲烷释放的缓解措施。

ABSTRACT: Atmospheric methane is a potent greenhouse gas that plays a major role in controlling the Earth's climate. The causes of the renewed increase of methane concentration since 2007 are uncertain given the multiple sources and complex biogeochemistry. Here, we present a metadata analysis of methane fluxes from all major natural, impacted and human-made aquatic ecosystems. Our revised bottom-up global aquatic methane emissions combine diffusive, ebullitive and/or plant-mediated fluxes from 15 aquatic ecosystems. We emphasize the high variability of methane fluxes within and between aquatic ecosystems and a positively skewed distribution of empirical data, making global estimates sensitive to statistical assumptions and sampling design. We find aquatic ecosystems contribute (median) 41% or (mean) 53% of total global methane

emissions from anthropogenic and natural sources. We show that methane emissions increase from natural to impacted aquatic ecosystems and from coastal to freshwater ecosystems. We argue that aquatic emissions will probably increase due to urbanization, eutrophication and positive climate feedbacks and suggest changes in land-use management as potential mitigation strategies to reduce aquatic methane emissions.
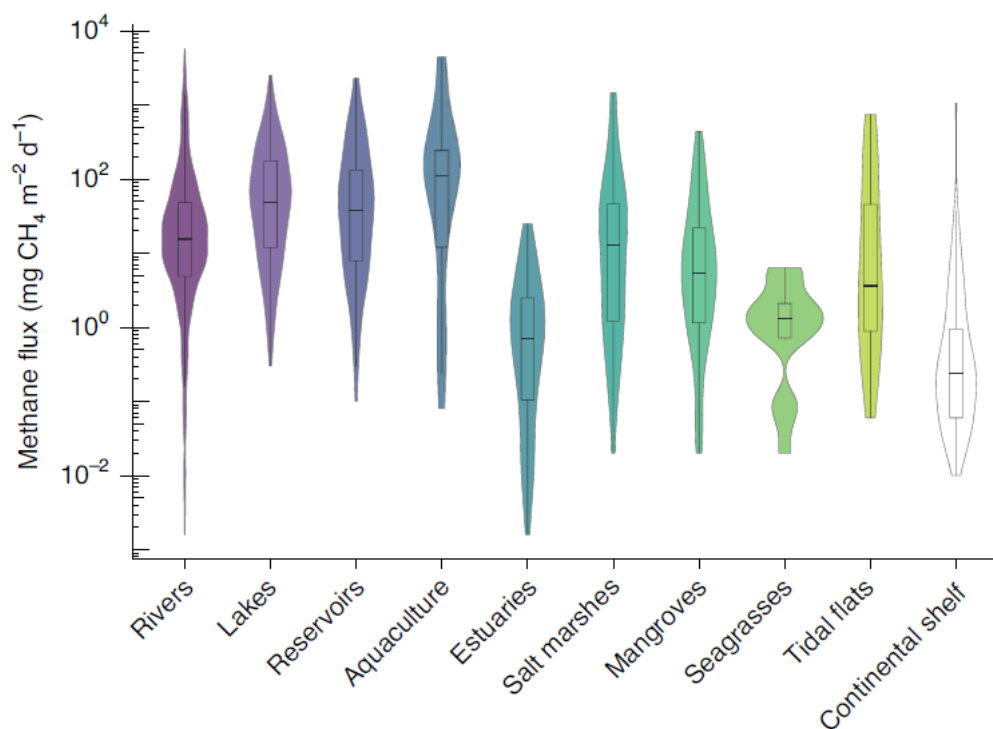

Figure 1. Inland water and coastal ocean areal methane fluxes. The violin plots include box plots showing median, lower (Q1) and upper (Q3) quartiles and 1.5 times the length of the interquartile range of methane fluxes from streams and rivers, lakes, reservoirs, aquaculture ponds (coastal and freshwater), estuaries, mangroves, salt marshes, seagrasses, tidal flats and continental shelves compiled in this study. Note the natural-log (ln) scale on the y-axis. All datasets (non-log transformed) are positively skewed (skewness coefficient >1, range 1.1 – 9.8).
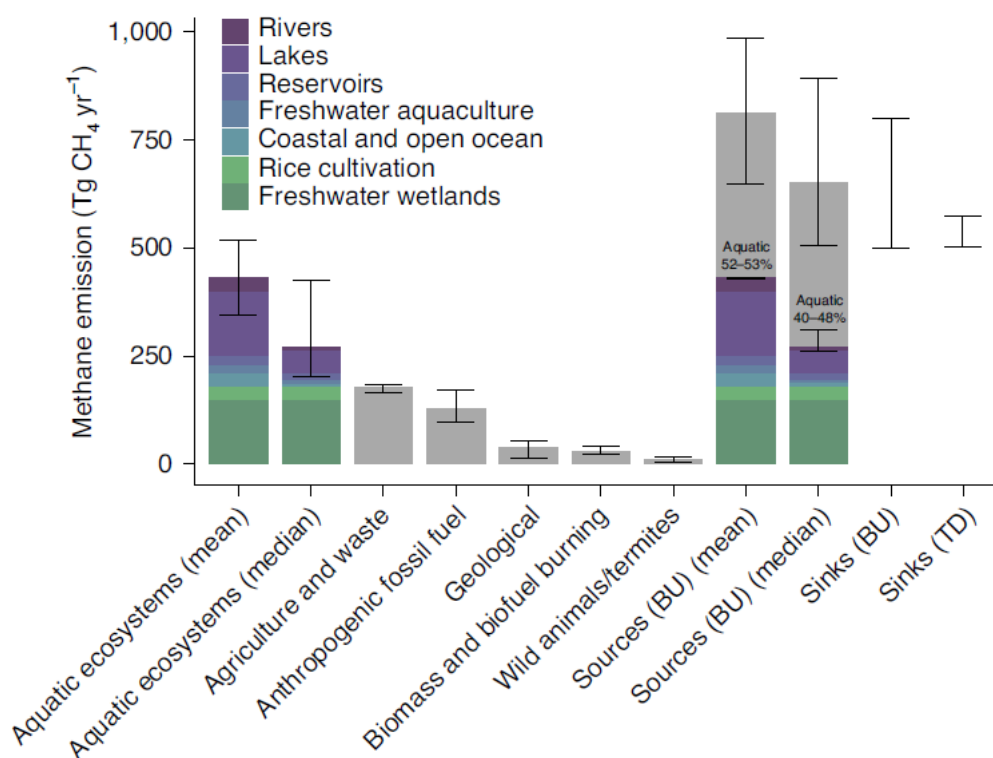
Figure 2. Global aquatic methane emissions compared with other global methane sources and sinks. Cumulative BU mean (IQR) and median (±c.i.95%) aquatic methane emissions estimated in this study compared with other BU methane sources versus BU and TD methane sinks from Saunois et al. (Table 2). The coastal and open ocean estimate includes emissions from estuaries, salt marshes, mangroves, seagrasses, tidal flats, coastal aquaculture ponds, continental shelves, continental slopes and the open ocean. Error estimates for freshwater wetland and rice emissions are based on inventory and biogeochemical modelling efforts, therefore showing comparably low variability and uncertainty.
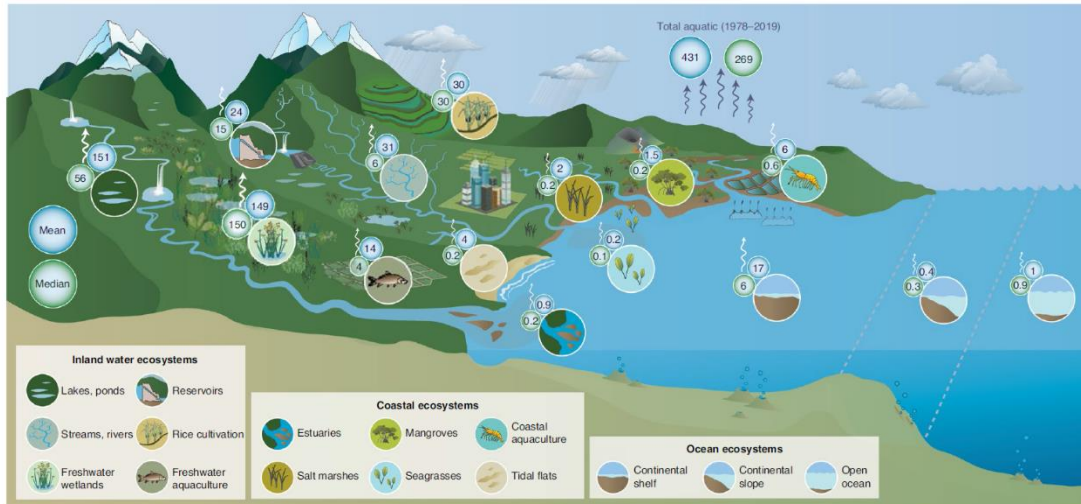
Figure 3. Global aquatic methane emissions from headwater streams to the open ocean. Numbers are Tg CH4 yr^{-1}. Mean emissions are shown in blue circles, and median emissions are shown in green circles. The relative importance of the factors controlling methane distribution and emissions varies along the land-ocean aquatic continuum.

4. 由于地幔最底部的高电导率太平洋地区地磁场变化异常低

翻译人：李园洁 liyj3@sustech.edu.cn

摘要：过去几个世纪以来，太平洋地区的地球磁场时间上变化异常低，这可能与核幔边界附近的液态外核内的大范围流动有关，其在太平洋下更弱，其主要特征是全球尺度的偏心环流，大体上避开这个区域。但是什么控制这种流动形态尚不清楚。本文，作者展示了地核内部动力学的数值模拟模型的结果，这种模型包含地幔底部的一个不均匀导电层的电磁耦合。当这个导电层的电导率在太平洋下面比其他区域更高时，更大的电磁拖曳力削弱局部地核流动，并使得全球尺度环流偏离太平洋。地幔底层电导率的本质还不清楚，但是核幔边界地形起伏中夹杂着分层地核流体是一种可能的解释。

ABSTRACT：For the past few centuries, the temporal variation in Earth's magnetic field in the Pacific region has been anomalously low. The reason for this is tied to large-scale flows in the liquid outer core near the core–mantle boundary, which are weaker under the Pacific and feature a planetary-scale gyre that is eccentric and broadly avoids this region. However, what regulates this type of flow morphology is unknown. Here we present results from a numerical model of the dynamics in Earth's core that includes electromagnetic coupling with a non-uniform conducting layer at the base of the mantle. We show that when the conductance of this layer is higher under the Pacific than elsewhere, the larger electromagnetic drag force weakens the local core flows and deflects the flow of the planetary gyre away from the Pacific. The nature of the lowermost mantle conductance remains unclear, but stratified core fluid trapped within topographic undulations of the core–mantle boundary is a possible explanation.
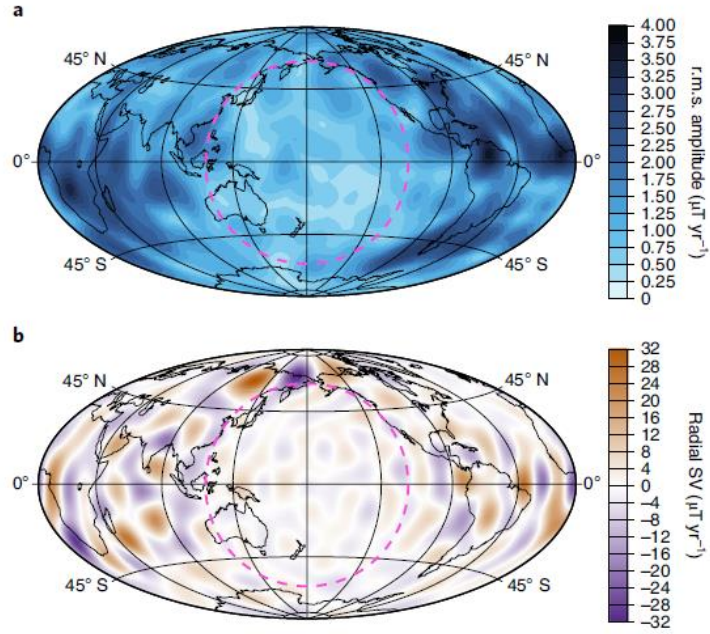
Figure 1. The low geomagnetic secular variation in the Pacific. a, The mean intensity of the radial component of the SV at the CMB, $|B_r|$, over the timeperiod 1590−1990 from the gufm field model[4]. The r.m.s. amplitude of $|B_r|$ in the Pacific (pink dashed circle) is 796.32 nT yr^{-1} while the global average is1,332.86 nT yr^{-1}, for a ratio of 0.5975. b, The radial component of the SV at the CMB, $|B_r|$, in 2015 from the CHAOS-6 field model[8] truncated at spherical harmonic degree 16. The r.m.s. amplitude of $|B_r|$ Iover the Pacific (pink dashed circle) is 2,034.13 nT yr^{-1} while the global average is 4,401.09nT yr^{-1}, for a ratio of 0.4622.
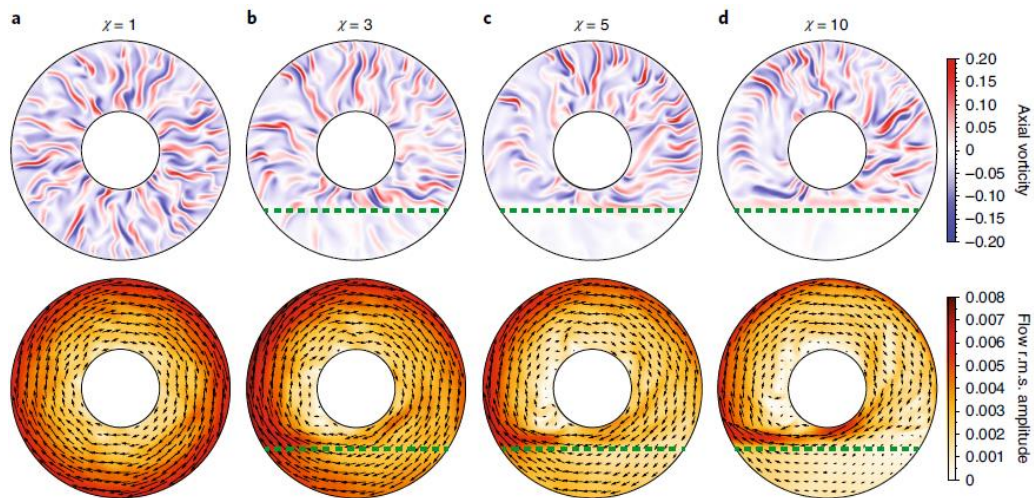

Figure 2. Modification of core flows by a non-uniform EM drag at the CMB. a–d, Snapshots of the axial

vorticity (top row) and time-averaged flow maps (bottom row; colour scale indicates flow speed, arrows show direction) from our quasi-geostrophic model for Ra = 5×10^8, Pm = 0.1 and χ = 1 (a), 3 (b),5 (c) and 10 (d). All plots are equatorial planforms. The Pacific region is shown in the bottom section of each planform, and is delimited by a dashed green line in b, c and d. The colour scales on the right are common to all four panels and are in non-dimensional units.

5. 受地幔源区不均一性影响的弧后盆地洋壳结构

翻译人：冯婉仪 fengwy@sustech.edu.cn

摘要： 俯冲带可能在火山弧后的上覆板块上形成海底扩张中心。在这种弧后环境下，俯冲板片控制着地幔对流的模式，并可能将含水熔体从火山弧或板片带入扩张脊熔融区。我们记录了横跨西马里亚纳洋脊（WMR，西北太平洋）的地震数据，这是一个两边都有弧后盆地的残余弧。它的边缘和两个盆地表现出明显不同的地壳结构。WMR 以西的帕里斯维拉盆地的地壳厚度为 4-5 km，并且其下地壳显示地震 P 波速度为 6.5-6.8 km/s。WMR 以东的马里亚纳海槽盆地的地壳厚度约为 7 km，其下地壳的地震速度为 7.2-7.4 km/s。其它弧后盆地的地震资料证实了这种结构多样性，这表明不同于正常洋中脊型地幔源区的地幔化学多样性和不均一性控制了弧后盆地的熔融程度。地幔的不均一性可能不仅仅是由含水熔体控制的，还可能是在俯冲带重新配置时冷的或亏损的地幔进入弧后的结果。因此，弧后盆地形成的地壳在厚度和速度结构上可能与正常洋壳不同。

ABSTRACT: Subduction zones may develop submarine spreading centers that occur on the overriding plate behind the volcanic arc. In these back-arc settings, the subducting slab controls the pattern of mantle advection and may entrain hydrous melts from the volcanic arc or slab into the melting region of the spreading ridge. We recorded seismic data across the Western Mariana Ridge (WMR, northwestern Pacific Ocean), a remnant island arc with back-arc basins on either side. Its margins and both basins show distinctly different crustal structure. Crust to the west of the WMR, in the Parece Vela Basin, is 4–5 km thick, and the lower crust indicates seismic P-wave velocities of 6.5–6.8 km/s. To the east of the WMR, in the Mariana Trough Basin, the crust is ~7 km thick, and the lower crust supports seismic velocities of 7.2–7.4 km/s. This structural diversity is corroborated by seismic data from other back-arc basins, arguing that a chemically diverse and heterogeneous mantle, which may differ from a normal

mid-ocean-ridge–type mantle source, controls the amount of melting in back-arc basins. Mantle heterogeneity might not be solely controlled by entrainment of hydrous melt, but also by cold or depleted mantle invading the back-arc while a subduction zone reconfigures. Crust formed in back-arc basins may therefore differ in thickness and velocity structure from normal oceanic crust.
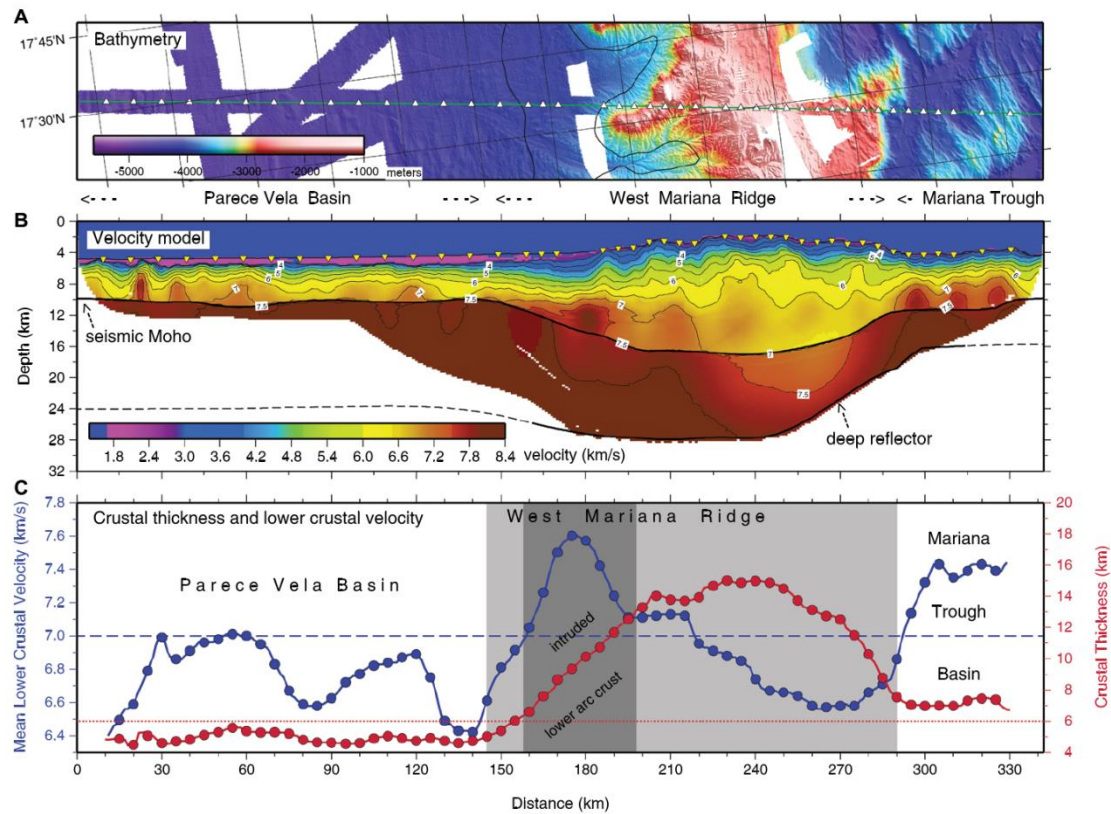

Figure 1. Seismic results from the West Mariana Ridge (northwestern Pacific Ocean). (A) Bathymetry along seismic profile MR101c across the West Mariana Ridge. (B) P-wave velocity model. (C) Mean lower-crustal velocity (blue) and crustal thickness (red). Reference velocity of 7 km/s for normal lower crust formed at mid-ocean ridges is shown by the blue dashed line; reference crustal thickness of 6 km is given by the dotted red line.
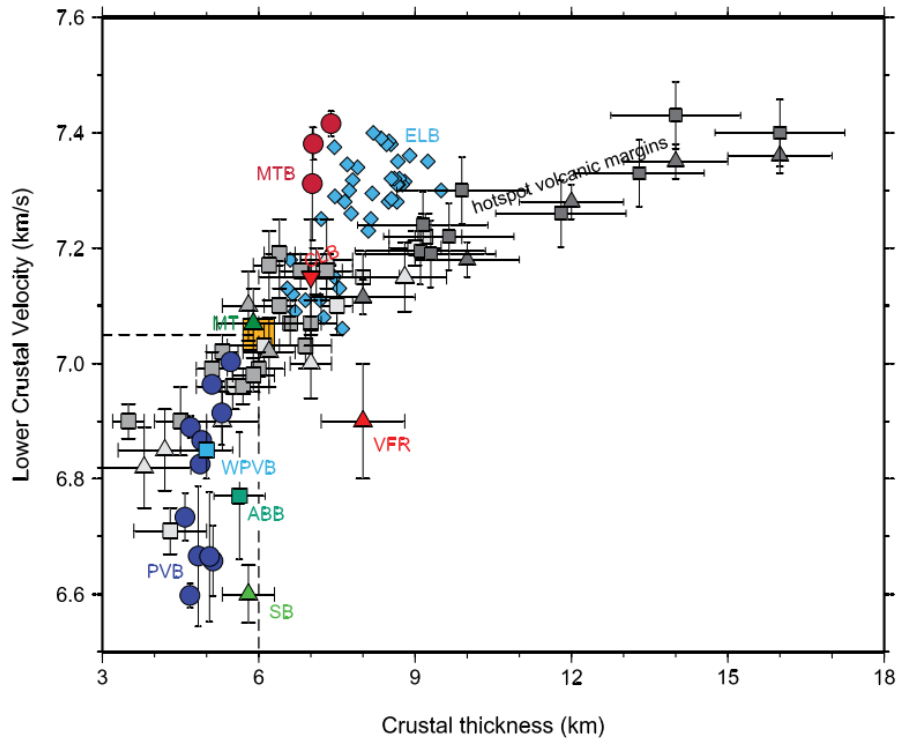
Figure 2. Classification of crust based on lowercrustal velocity and crustal thickness; melting of pyrolytic mantle at normal mantle temperature should form 6-km-thick oceanic crust (orange square; Sallares et al., 2005). Depending on the tectonic setting, oceanic crust may deviate from the reference as indicated by the gray symbols (light gray—slow and ultraslow spreading ridges; gray—fast spreading ridges [Grevemeyer et al., 2018]; dark gray—hotspot provinces [Hopper et al., 2003; White et al., 2008]). Colored symbols are back-arc spreading centers: blue circles—Parece Vela Basin (PVB, northwestern Pacific Ocean; this study); red circles—Mariana Trough Basin (MTB; this study); light blue diamonds—Eastern Lau Basin (ELB, southwestern Pacific Ocean; Arai and Dunn, 2014); green triangle—Mariana Trough spreading center (MT; Takahashi et al., 2008); blue square—western Parece Vela Basin (WPVB; Nishizawa et al., 2007); light green triangle—Shikoku Basin (SB; Nishizawa et al., 2011); green square—Algerian-Balearic Basin (ABB, western Mediterranean Sea; Booth-Rea et al., 2018); red triangle—Valu Fa Ridge in the southern Lau Basin (VFR; Turner et al., 1999); red inverted triangle—Central Lau Basin (CLB; Crawford et al., 2003).

6. 海沟轴向水道形成与演化的控制因素

翻译人：刘伟 inewway@163.com

*McArthur A D, Tek D E. **Controls on the origin and evolution of deep-ocean trench-axial channels**[J]. Geology, 2021.*

https://doi.org/10.1130/G48612.1

摘要： 进入俯冲带的沉积物类型和体积影响着板块边界变形的样式，从而影响沉积旋回和构造旋回。由于海底水道可显著提高浊流的输运效率，因此俯冲海沟中水道的存在与否是影响海沟充填的主要因素。到目前为止，对海沟轴向水道的结构特征还不是太了解，这不利于研究其形成和演化的控制因素。在这里，我们描述了 Hikurangi 水道的演化，它穿过 Hikurangi 海沟，位于新西兰近海。对二维和三维地震资料的分析表明，该水道的存在时间仅在最近的 3.5 m.y.，而海沟的存在时间则持续 27 m.y.。水道的产生和演变是由于陆源区的剥蚀增加导致了海沟沉积物供给的增加。为了验证对 Hikurangi 水道演化的控制因素是否具有普遍性，本文利用全球俯冲海沟地貌的多元统计分析，研究了现代海沟中轴向海沟的形成条件。海沟中陆源沉积物的供给和沉积物覆盖厚度是主要的控制因素；而辅助因素，如海沟长度和海沟的凹凸不平也有助于轴向水道的演化。轴向水道调节着海沟内的泥沙分布，并且随着海沟的演化而在时间和空间上发生变化。轴向水道的存在影响着板块边界力学，并对俯冲边缘变形形式有影响。

ABSTRACT: The type and volume of sediment entering subduction zones affects the style of plate-boundary deformation and thus sedimentary and tectonic cycles. Because submarine channels significantly increase the transport efficiency of turbidity currents, their presence or absence in subduction trenches is a primary control on trench fill. To date, comprehensive architectural characterization of trench-axial channels has not been possible, undermining efforts to identify the factors controlling their initiation and evolution. Here, we describe the evolution of the Hikurangi Channel, which traverses the Hikurangi Trench, offshore New Zealand. Analysis of two- and three-

dimensional seismic data reveals that the channel was present only during the last ~3.5 m.y. of the ~27 m.y. of the trench's existence; its inception and propagation resulted from increased sediment supply to the trench following amplified hinterland exhumation. To test if the controls on the evolution of the Hikurangi Channel are universal, multivariate statistical analysis of the geomorphology of subduction trenches globally is used to investigate the formative conditions of axial channels in modern trenches. Terrigenous sediment supply and thickness of sediment cover in a trench are the dominant controls; subsidiary factors such as trench length and rugosity also contribute to the conditions necessary for trench-axial channel development. Axial channels regulate sediment distribution in trenches, and this varies temporally and spatially as a channel propagates along a trench. The presence of a trench-axial channel affects plate-boundary mechanics and has implications for the style of subduction-margin deformation.
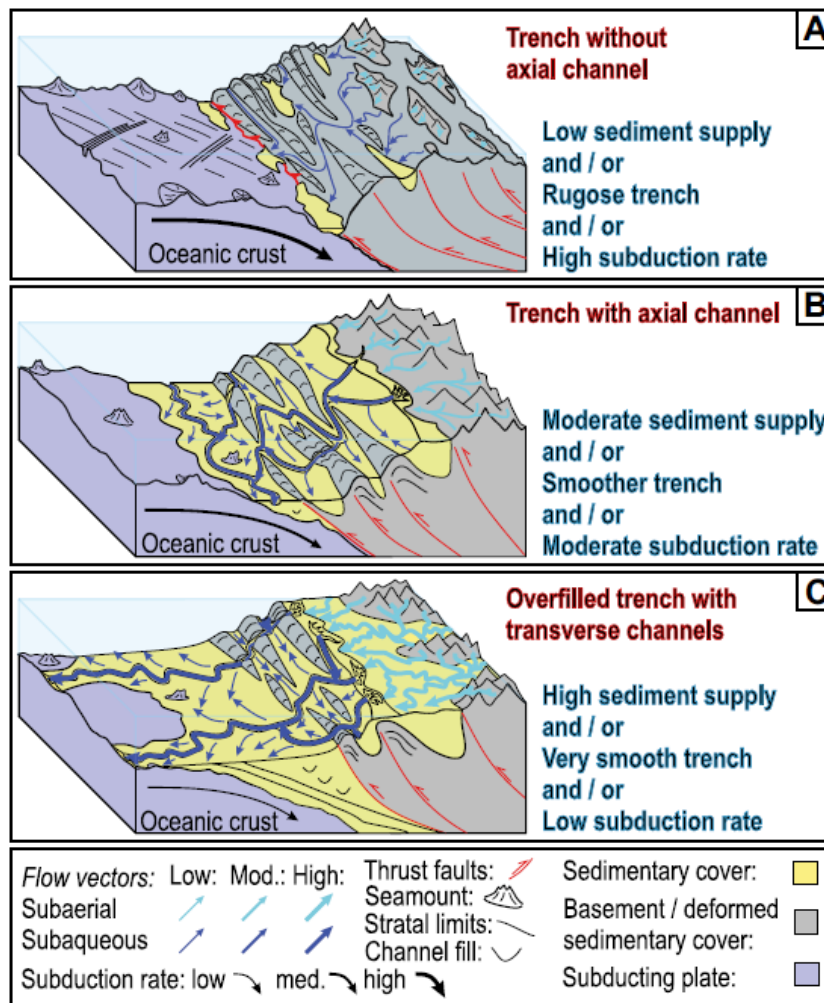

Figure 1. Schematic representation of controls on trench fill and axial-channel evolution. Mod.— moderate; med.—medium.

7. 西风急流的位置和方向决定了中国全新世降雨模式

翻译人：杨会会 11849590@mail.sustech.edu.cn

摘要：基于气候指标重建的中国和蒙古全新世时空降水模式和模拟结果相互矛盾，表明东亚夏季风及其与西风急流相互作用的基本机制尚不清楚。我们从 101 个化石花粉记录中对全新世降水进行了定量重建，并利用最小经验模型对其进行了分析。结果表明，全新世中期以来，西风急流轴逐渐向南移动，倾斜程度降低。夏季风雨带导致全新世早期降雨最大值覆盖了中国西部大部分地区，全新世中期最大降水则出现在中国中北部和东北地区，而全新世晚期最大降水出现在中国东南部。我们的结果表明，正确模拟西风急流的方向和位置对准确预测中国和蒙古地区的降水模式至关重要。

ABSTRACT: Proxy-based reconstructions and modeling of Holocene spatiotemporal precipitation patterns for China and Mongolia have hitherto yielded contradictory results indicating that the basic mechanisms behind the East Asian Summer Monsoon and its interaction with the westerly jet stream remain poorly understood. We present quantitative reconstructions of Holocene precipitation derived from 101 fossil pollen records and analyze them with the help of a minimal empirical model. We show that the westerly jet-stream axis shifted gradually southward and became less tilted since the middle Holocene. This was tracked by the summer monsoon rain band resulting in an early-Holocene precipitation maximum over most of western China, a mid-Holocene maximum in north-central and northeastern China, and a late-Holocene maximum in southeastern China. Our results suggest that a correct simulation of the orientation and position of the westerly jet stream is crucial to the reliable prediction of precipitation patterns in China and Mongolia.
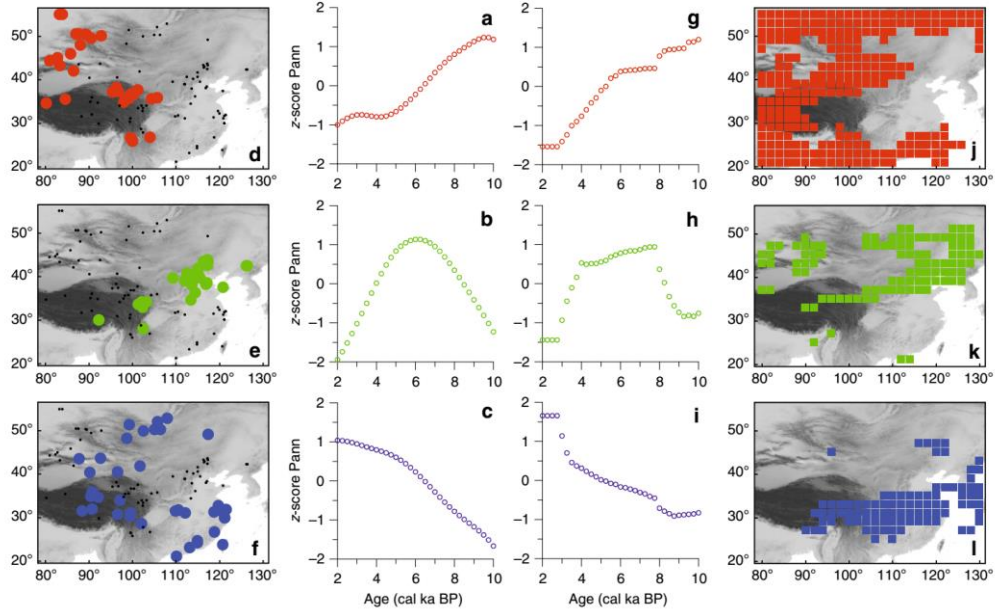
Figure 1. Holocene precipitation patterns for eastern Asia derived from clustering of Holocene time-series of pollen-inferred and simulated annual precipitation. a–c (pollen-infered) and g–i (simulated) show temporal variations in the centers of each cluster, as derived from unsupervised fuzzy competitive learning (see Methods). d–f Show the spatial distribution of pollen-inferred time-series that have a membership degree >0.5 to a particular cluster. j–l Show the spatial distribution of simulated time-series that have a membership degree >0.5 to a particular cluster
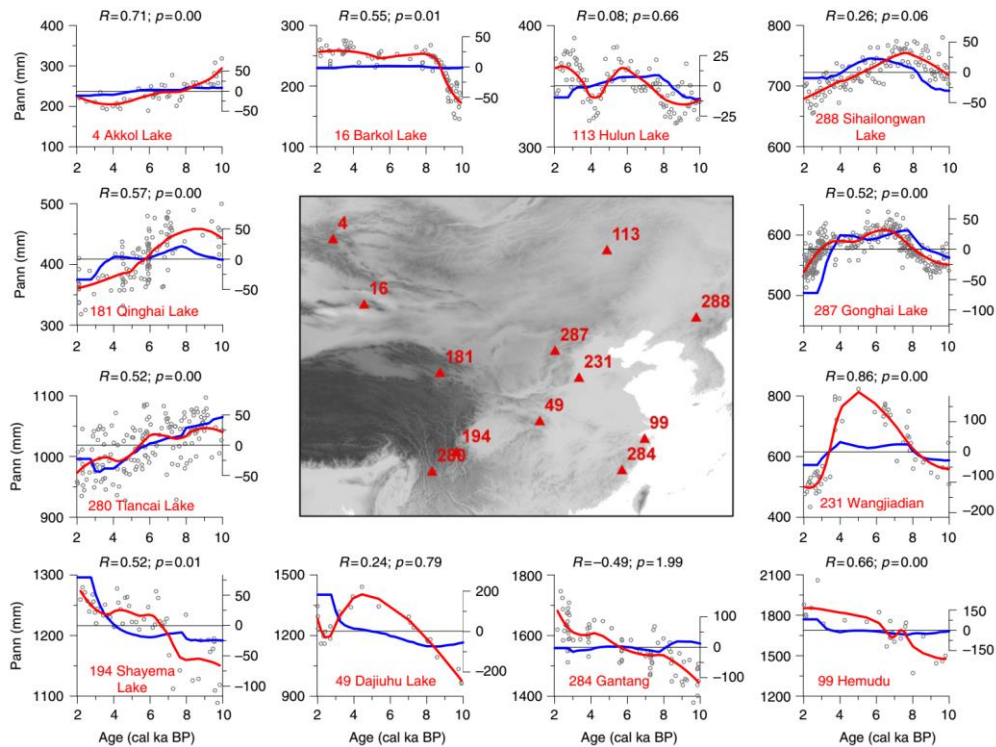
Figure 2. Reconstructed and simulated precipitation of selected sites in China and Mongolia. Pollen-based reconstructions of annual precipitation (mm/year; black circles are original data points, red lines is loess smoothed values (span: 0.5, left scale) compared to simulated precipitation anomalies (mm/year, blue lines, right scale) using a minimal empirical model of selected sites. Correlation coefficient and p-values are indicated (i.e., between loess-smoothed reconstructions and simulated time-series from the respective grid-cell). Central map shows the locations of the sites: only sites that had a sufficiently high-resolution and a reliable age model were selected (see Supplementary Table 3 for further details). (Note axes are not on the same scale.)
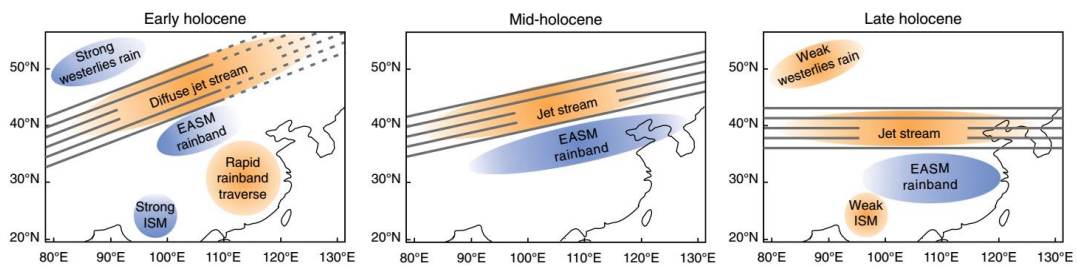

Figure 3. Sketch maps of eastern Asia showing the major summer precipitation and circulation characteristics for early, middle, and late Holocene. Original results were derived by applying pollen-based transfer functions to 101 fossil pollen records and using a minimal empirical model based on present-day relationships between insolation, the position of the westerly jet stream, and spatial distribution patterns for precipitation. (EASM—East Asian Summer Monsoon, ISM—Indian Summer Monsoon)

8. 火星上地壳磁化成分的增强

翻译人：曹伟 11930854@QQ.com

摘要：火星轨道和着陆器探测的结果显示，火星具有强的（比地球大 1-2 个数量级）地壳磁异常并且缺少可检测到的活跃地核发电机。考虑到火星古地核发电机预测模型的地表磁场强度与现代地球相当，这种强烈的地壳磁化仍然无法解释。我们在多元空间中探索了火星地壳磁化强度与其组成的关系。我们发现，在 Terra Sirenum-Terra Cimmeria 地区，530 和 1000nm 吸收（轨道光谱仪）与地壳磁化强度存在独特的相关性，磁化强度 13% 的变化可以归因于这些相关性。我们并不指望轨道光谱仪探测的表层物质可以保留古地核发电机的磁场，所以我们认为这种磁性材料在成份上类似于深部的大块岩石，它更有可能记录到剩磁，因此我们观测到的变化应该来源于深部。

ABSTRACT: Martian orbital and lander measurements revealed strong (1-2) orders of magnitude greater than Earth) crustal magnetic anomalies and the lack of an active detectable core dynamo. This strong crustal magnetization remains unexplained given that models of an ancient core dynamo on Mars predict surface field strengths comparable to modern Earth. We explored the relationship between Mars' crustal magnetization and its composition in multivariate space. We identified that 530 and 1,000 nm absorptions (from orbital spectrometers) have unique correlations with crustal magnetization in the Terra Sirenum-Terra Cimmeria region and 13% of the variance of the magnetization can be attributed to these correlations. Because we do not expect the topmost material, detectable by the orbital spectrometers, to retain magnetization from an ancient core dynamo, we propose this material is compositionally similar to the bulk rock below it, which is more likely to retain magnetization. Therefore, the observed variance is a lower limit.
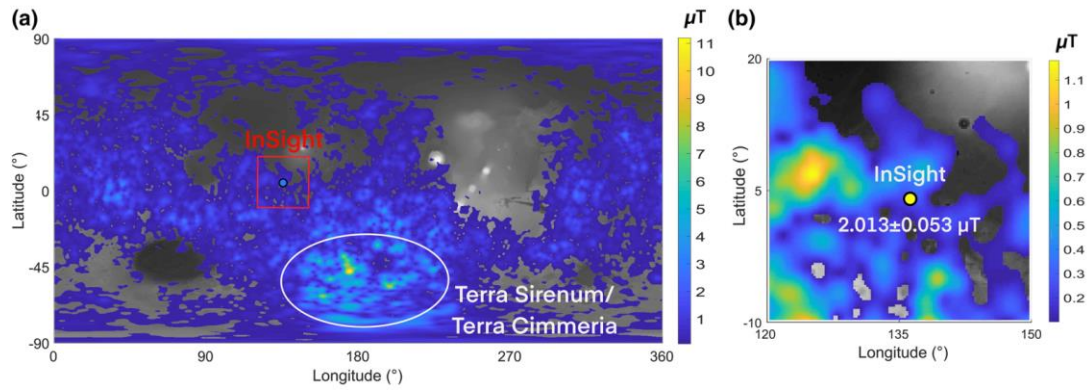
Figure 1. (a) Surface magnetic field prediction at 4 pixels/degree calculated using Langlais et al. (2019), regions where the predicted surface field was below 100 nT are excluded. Background is MOLA topography. (b) InSight result from Johnson et al. (2020) are shown above the predicted values.

9. 硅酸盐、碳酸盐和硫化物风化作用的协同变化驱动了 CO_2 随侵蚀作用的释放

翻译人：张伟杰 12031188@mail.sustech.edu.cn

摘要:全球气候被认为是受地表矿物供应的调节。硅酸盐风化作用减少了大气中的二氧化碳，而碳酸盐和硫化物矿物风化作用是地质相关的二氧化碳来源。这些风化路径通常是一起进行的，但它们关于侵蚀速率梯度的协同变化缺乏定量约束。本研究以台湾南部泥页岩及砂岩为研究对象，通过三个数量级的侵蚀速率梯度研究，发现硫化物及碳酸盐风化速率随侵蚀程度增加而上升，而硅酸盐风化速率则保持稳定。因此，在比海洋硫化物补偿时间(大约 $10^6 \sim 10^7$ 年)短的时间尺度上，快速侵蚀地形的风化导致净二氧化碳排放速率至少是缓慢侵蚀地形的 CO_2 封存速率的两倍。我们认为这些风化反应是相互关联的，由硫化物氧化生成的硫酸可以提高碳酸盐的可溶性，可能是由于 pH 值的有效缓冲作用，硅酸盐风化动力学则不受影响。我们认为，这些模式广泛适用于许多含有海相变质沉积岩的新生代山脉。

ABSTRACT: Global climate is thought to be modulated by the supply of minerals to Earth's surface. Whereas silicate weathering removes carbon dioxide (CO_2) from the atmosphere, weathering of accessory carbonate and sulfide minerals is a geologically relevant source of CO_2. Although these weathering pathways commonly operate side by side, we lack quantitative constraints on their co-variation across erosion rate gradients. Here we use stream-water chemistry across an erosion rate gradient of three orders of magnitude in shales and sandstones of southern Taiwan, and find that sulfide and carbonate weathering rates rise with increasing erosion, while silicate weathering rates remain steady. As a result, on timescales shorter than marine sulfide compensation (approximately 10^6–10^7 years), weathering in rapidly eroding terrain leads to net CO_2 emission rates that are at least

twice as fast as CO_2 sequestration rates in slow-eroding terrain. We propose that these weathering reactions are linked and that sulfuric acid generated from sulfide oxidation boosts carbonate solubility, whereas silicate weathering kinetics remain unaffected, possibly due to efficient buffering of the pH. We expect that these patterns are broadly applicable to many Cenozoic mountain ranges that expose marine metasediments.
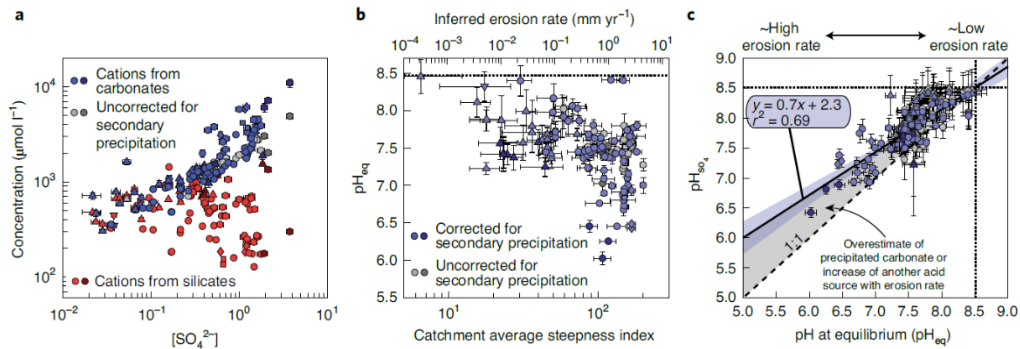

Figure 1. Link between sulfuric acid, weathering and pH. a, Co-variation of cation concentrations with sulfate. b, Predicted maximum pH in the weathering zone (pH_{eq}) against catchment-averaged steepness index (lower x axis) and inferred erosion rates (upper x axis). c, Predicted pH for a carbonate-buffered solution after addition of sulfuric acid (pH_{SO4}) against the equilibrium pH. The solid line shows regression with 95% confidence bands; the dotted lines show initial pH before addition of sulfuric acid. Symbols mark dominant lithology (see Fig. 1). Error bars are equivalent to a 95% confidence interval. Samples with anomalously high sulfate concentrations are marked as darker points.
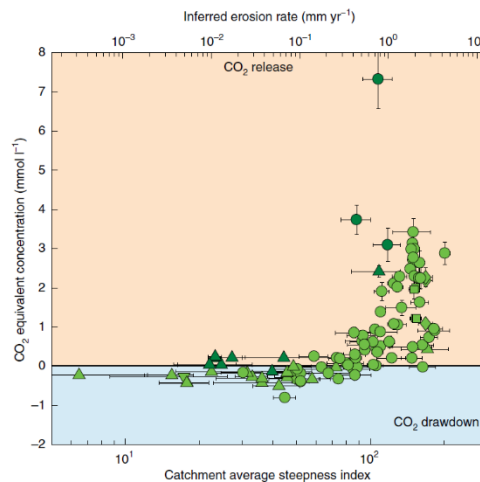

Figure 2. Impact of erosion on the long-term carbon cycle. Moles of CO_2 emitted or sequestered per

volume of water against catchment-averaged steepness index (lower x axis) and inferred erosion rates (upper x axis). Symbols mark dominant lithology (see Fig. 1). Error bars are equivalent to a 95% confidence interval. Samples with anomalously high sulfate concentrations are marked as darker points.

10. 解析格陵兰冰芯记录中气候突然变暖的信息

翻译人：李海 12031330@mail.sustech.edu.cn

摘要：数据的可靠性和时间分辨率是制约更好揭示末次冰期气候突变的特征（持续时间和阶段）的主要因素。本次研究，作者利用年代分辨为 10 年的格陵兰冰芯记录剖析气候突变的特征。作者着重指出在不同的冰芯参数中记录的突变信息并未展现系统的模式。冰芯参数变化的多样性也可从数值模拟出的气候参数中观察到，这些参数显示出由于内部大气-冰-海相互作用而产生自身维持的突变。作者对两个冰芯进行分析后指出，气候突然变暖的多样性代表了气候系统固有的可变性，而不是沉积记录中的噪声。研究结果表明，在这些气候突变期，由于气候系统的紧密耦合，可能无法推断出冰芯参数中记录的气候突变发生的准确时间。

ABSTRACT: Data availability and temporal resolution make it challenging to unravel the anatomy (duration and temporal phasing) of the Last Glacial abrupt climate changes. Here, we address these limitations by investigating the anatomy of abrupt changes using sub-decadal-scale records from Greenland ice cores. We highlight the absence of a systematic pattern in the anatomy of abrupt changes as recorded in different ice parameters. This diversity in the sequence of changes seen in ice-core data is also observed in climate parameters derived from numerical simulations which exhibit self-sustained abrupt variability arising from internal atmosphere-ice-ocean interactions. Our analysis of two ice cores shows that the diversity of abrupt warming transitions represents variability inherent to the climate system and not archive-specific noise. Our results hint that during these abrupt events, it may not be possible to infer statistically-robust leads and lags between the different components of the climate system because of their tight coupling.
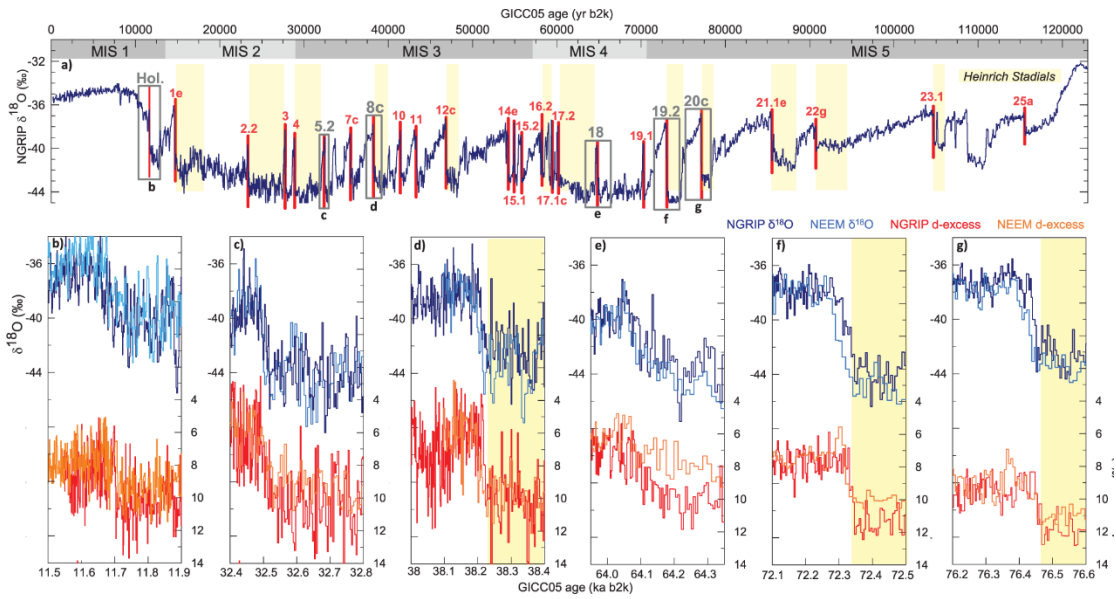
Figure 1. Abrupt climate variability recorded in Greenland water isotopic records. a NGRIP δ¹⁸O record5. Studied abrupt warming transitions are highlighted with red vertical bars and Greenland Interstadials (GI) are numbered. Gray boxes indicate intervals shown in (b–g), illustrating the variety of abrupt GS–GI transitions across the Last Glacial; stadials containing Heinrich events are indicated in yellow following refs. and Marine Isotope Stages (MIS) are indicated in gray. b–g High-resolution δ¹⁸O from NGRIP (dark blue) and NEEM (light blue) and d-excess from NGRIP (red) and NEEM (orange) over 400 yr time intervals centered on the Holocene abrupt onset (b) and the abrupt transitions into GI-5.2 (c), GI-8c (d), GI-18 (e), GI-19.2 (f), and GI-20c (g).
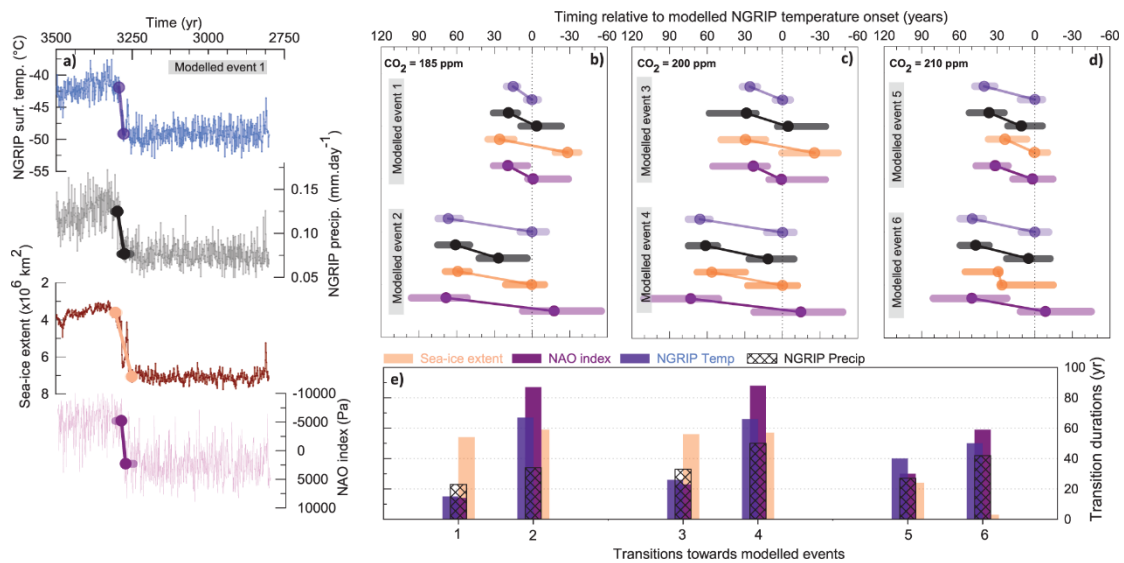

Figure 2. Anatomy of self-sustained abrupt transitions simulated in CCSM4. Onset and endpoints (dots) of modeled abrupt transitions (oblique lines) together with associated uncertainty intervals (horizontal

shaded lines) found by the ramp-fitting analysis on time series of the annual surface air temperature (blue) and the annual precipitation rate (black) both at the model grid point closest to NGRIP, the sea-ice extent in the Irminger Seas (light orange) and an NAO index defined as PC1 of sea-level pressure variations in the North Atlantic region (purple; details in SOM) over the two unforced oscillations simulated in CCSM4 with atmospheric CO_2 concentrations of (a–b) 185 ppm, (c) 200 ppm, and (d) 210 ppm. The time series (numbered 1–6) are shown in Supplementary Figure 7. (a) simulated time series for each climate parameter from the first modeled abrupt change under a CO_2 concentration background of 185 ppm are represented together with the resulting identification of the onset and the end of the abrupt transition from the ramp-fitting analysis to illustrate what is represented in (b–d). All transitions are shown relative to the timing of the onset of the NGRIP surface air temperature transition (dashed vertical line). The vertical amplitude between the onset and the end of each transition is the same for all tracers, it has been set arbitrarily and does not represent the true amplitude of change for each ice-core tracer. (e) Zoom on the duration estimates of the transitions in the simulated climatic parameters. Uncertainty intervals in the transition duration range from 15 to 118 yr with a mean of 57 yr (they are omitted here for clarity purposes).

11. 湖相碳酸盐岩地层碎屑锆石 U-Pb 年代学研究

翻译人：周洋 zhouy3@sustech.edu.cn

摘要：非海洋系统中的湖相碳酸盐岩地层具有通过碎屑锆石 U-Pb 定年测定沉积年龄的巨大潜力。在碳酸盐沉积环境中，碎屑沉积物通量较低，可能会增加火山灰沉积锆石的相对比例，从而增加了通过碎屑锆石年龄观察到真实沉积年龄的机会。我们介绍了湖相碳酸盐岩地层碎屑锆石的 U-Pb 年代学，这为解决非海洋地层沉积年龄提供了依据。本次研究的样品采集自美国 Montana 西南部的早白垩世前陆盆地河流相砂岩和湖相碳酸盐岩。晚 Aptian-早 Albian 期（约 115-110 Ma）上段沉积的最大沉积年龄与生物地层年龄一致。湖相碳酸盐是许多构造盆地重要组成部分，碎屑锆石 U-Pb 年代学的应用在确定地层中记录的关键地球化学和气候事件具有相当大的潜力。它还可以揭示一些新信息，地层记录是以较长期的细粒沉积还是以短时期的粗粒沉积为主。在构造盆地中，它也可能为构造沉降（特别是泥岩和碳酸盐为主的细粒沉积）的初始时间提供依据。

ABSTRACT: Carbonate lacustrine strata in nonmarine systems hold great potential for refning depositional ages through U-Pb dating of detrital zircons. The low clastic sediment flux in carbonate depositional environments may increase the relative proportion of zircons deposited by volcanic air fall, potentially increasing the chances of observing detrital ages near the true depositional age. We present U-Pb geochronology of detrital zircons from lacustrine carbonate strata that provides proof of concept for the effectiveness of both acid-digestion recovery and resolving depositional ages of nonmarine strata. Samples were collected from Early Cretaceous foreland basin fluvial sandstone and lacustrine carbonate in southwestern Montana (USA). Late Aptian–early Albian (ca. 115–110 Ma) maximum depositional ages young upsection and agree with biostratigraphic ages. Lacustrine carbonate is an important

component in many types of tectonic basins, and application of detrital zircon U-Pb geochronology holds considerable potential for dating critical chemical and climatic events recorded in their stratigraphy. It could also reveal new information for the persistent question about whether the stratigraphic record is dominated by longer periods of background fne-grained sedimentation versus short-duration coarse-grained events. In tectonically active basins, lacustrine carbonates may be valuable for dating the beginning of tectonic subsidence, especially during periods of fner-grained deposition dominated by mudrocks and carbonates.
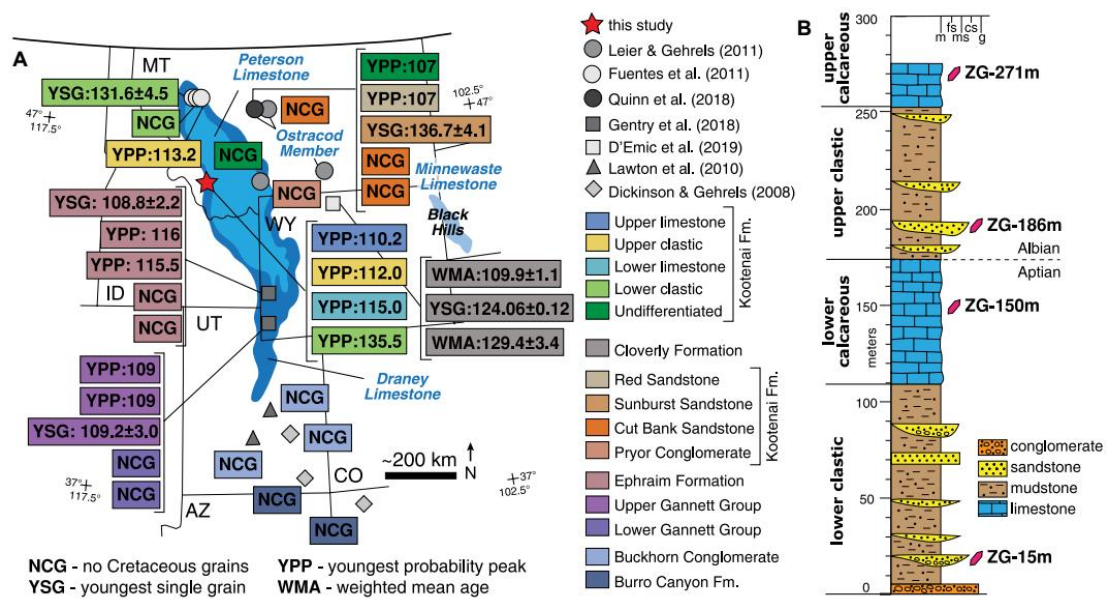

Figure 1. (A) Locations of detrital zircon samples and maximum depositional ages (in Ma) of Lower Cretaceous strata, western United States. MT—Montana; WY—Wyoming; ID—Idaho; UT—Utah; CO—Colorado; AZ—Arizona. (B) Measured stratigraphic section of the Kootenai Formation at Ziegler Gulch, Montana, with positions of detrital zircon samples from this study. m—mudstone; fs—fne-grained sandstone; ms—mediumgrained sandstone; cs—coarse-grained sandstone; g—gravel.

12. 火星上类似陆地源-汇系统的盖尔环形山古气候

翻译人：张琪 zhangq7@sustech.edu.cn

摘要: 晚诺亚纪到早赫斯珀利亚纪期间，河流将火成岩碎屑运送到下游盖尔火山口里的湖泊，形成了堆叠起来且分层的河流湖沼成因岩石，出露在夏普山的斜坡上。关于支持盖尔环形山液态水地表径流的古气候研究存在争议，这在很大程度上是因为人们对从基性岩石为主的源-汇系统中化学和矿物学的古气候指标如何转化为岩石记录知之甚少。在这里，我们收集了来自地球上不同气候类型地区的玄武岩地形数据，以便为盖尔环形山沉积层形成期间可能的气候条件提供一个参考框架，特别是 Sheepbed 和 Pahrump Hills 地区。我们通过计算风化剖面和河流沉积物的化学蚀变指数来更好地约束基性地形中气候与化学风化的关系，这是一种最好地估算平均降温极限的方法。我们还比较了不同陆地气候类型地区的河流沉积物和火星泥岩的 X 射线衍射谱和矿物丰度，以更好地了解气候对玄武岩地形中次生矿物组合的影响。我们发现，盖尔环形山大部分细粒沉积岩的地球化学和矿物学特征与现在冰岛的沉积物具有一级相似性，而其他地层指示了更冷的基线气候条件。盖尔环形山的岩性特征没有任何一个地方被检测出来与陆地上温暖地区的河流沉积物或风华剖面相似。

ABSTRACT: In the Late Noachian to Early Hesperian period, rivers transported detritus from igneous source terrains to a downstream lake within Gale crater, creating a stratified stack of fluviolacustrine rocks that is currently exposed along the slopes of Mount Sharp. Controversy exists regarding the paleoclimate that supported overland flow of liquid water at Gale crater, in large part because little is known about how chemical and mineralogical paleoclimate indicators from mafic-rock dominated source-to-sink systems are translated into the rock record. Here, we compile data from basaltic terrains with varying climates on Earth in order to provide a reference frame for the

conditions that may have prevailed during the formation of the sedimentary strata in Gale crater, particularly focusing on the Sheepbed and Pahrump Hills members. We calculate the chemical index of alteration for weathering profiles and fluvial sediments to better constrain the relationship between climate and chemical weathering in mafic terrains, a method that best estimates the cooler limit of climate conditions averaged over time. We also compare X-ray diffraction patterns and mineral abundances from fluvial sediments in varying terrestrial climates and martian mudstones to better understand the influence of climate on secondary mineral assemblages in basaltic terrains. We show that the geochemistry and mineralogy of most of the fine-grained sedimentary rocks in Gale crater display first-order similarities with sediments generated in climates that resemble those of present-day Iceland, while other parts of the stratigraphy indicate even colder baseline climate conditions. None of the lithologies examined at Gale crater resemble fluvial sediments or weathering profiles from warm (temperate to tropical) terrestrial climates.
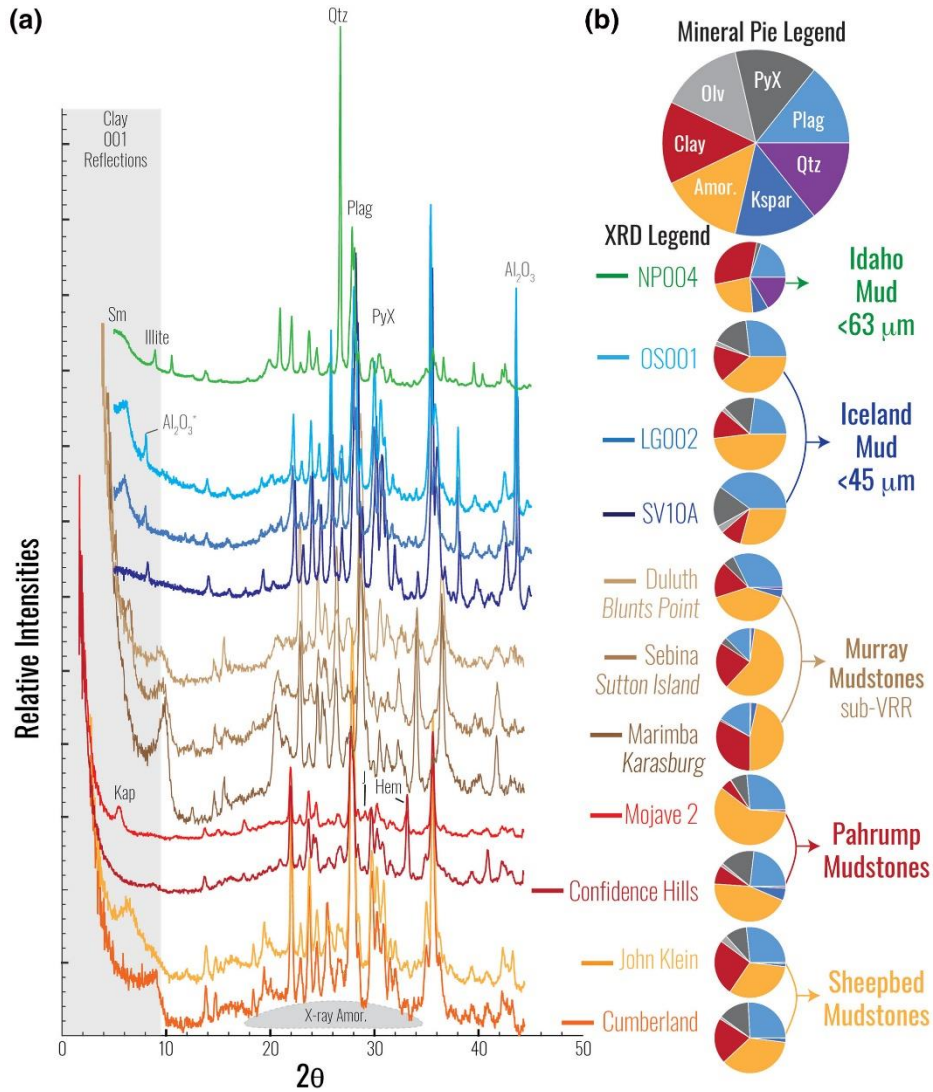
Figure 1. XRD patterns for two Sheepbed mudstones (Vaniman et al., 2014), two Pahrump Hills mudstones (Rampe, Ming, et al., 2017), three mudstones from the Murray formation between Pahrump Hills and Vera Rubin ridge (sub-VRR) (Bristow et al., 2018; Rampe et al., 2020), the <45- μ m sediment from Iceland (M. T. Thorpe et al., 2019), and a <63- μ m sediment sample from the Idaho (M. T. Thorpe & Hurowitz, 2020) sample suite (a). Martian target names and terrestrial analog sample IDs are next to the XRD patterns. In (b), pie charts display the mineral group abundances for these terrestrial muds and martian mudstones. First-order similarities are observed in the XRD patterns for Iceland and Gale crater mudstones, including clay mineral reflections at low-two theta, sharp, well-resolved peaks from primary minerals (esp., plagioclase and pyroxene) sharp peaks, and an elevated background from the scatter produced from an X-ray amorphous phase(s). Mineral abundances between Iceland mud and Gale crater mudstones also show similarities. XRD pattern and pie chat abbreviations: plagioclases (Plag);

pyroxenes (Pyx); olivines (Olv); smectites (sm); smectite, illite, and kaolinite (Clay); quartz (Qtz); X-ray amorphous (X-ray Amor or just Amor); hematite (Hem); jarosite (J); kapton window (Kap); Al2O3 internal standard in Icelandic samples accounts for <1 wt% of total derived mineral abundances.